TWO-TIER TISSUE DECOMPOSITION FOR HISTOPATHOLOGICAL IMAGE REPRESENTATION AND CLASSIFICATION

A THESIS

SUBMITTED TO THE DEPARTMENT OF COMPUTER ENGINEERING

AND THE GRADUATE SCHOOL OF ENGINEERING AND SCIENCE

OF BILKENT UNIVERSITY

IN PARTIAL FULFILLMENT OF THE REQUIREMENTS

FOR THE DEGREE OF

MASTER OF SCIENCE

By

Tunç Gültekin

April, 2014

I certify that I have read this thesis and that in my opinion it is fully adequate, in scope and in quality, as a thesis for the degree of Master of Science.

Assoc. Prof. Dr. Çiğdem Gündüz Demir(Advisor)

I certify that I have read this thesis and that in my opinion it is fully adequate, in scope and in quality, as a thesis for the degree of Master of Science.

Prof. Dr. Billur Barshan

I certify that I have read this thesis and that in my opinion it is fully adequate, in scope and in quality, as a thesis for the degree of Master of Science.

Assoc. Prof. Dr. Selim Aksoy

Approved for the Graduate School of Engineering and Science:

Prof. Dr. Levent Onural
Director of the Graduate School

ABSTRACT

TWO-TIER TISSUE DECOMPOSITION FOR HISTOPATHOLOGICAL IMAGE REPRESENTATION AND CLASSIFICATION

Tunç Gültekin
M.S. in Computer Engineering
Supervisor: Assoc. Prof. Dr. Çiğdem Gündüz Demir
April, 2014

In digital pathology, devising effective image representations is crucial to design robust automated diagnosis systems. To this end, many studies have proposed to develop object-based representations, instead of directly using image pixels, since a histopathological image may contain a considerable amount of noise typically at the pixel-level. These previous studies mostly define their objects, based on the color information, as to approximately represent histological tissue components in an image and then use the spatial distribution of these objects for image representation and classification. Thus, object definition has a direct effect on the way of representing the image, which in turn affects classification accuracies. In this thesis, we present a new model for effective representation and classification of histopathological images. The contributions of this model are twofold. First, it introduces a new two-tier tissue decomposition method for defining a set of multi-typed objects in an image. Different than the previous studies, these objects are defined combining the texture, shape, and size information and they may correspond to individual histological components as well as tissue sub-regions of different characteristics. As its second contribution, it defines a new metric, which we call "dominant blob scale", to characterize the shape and size of an object with a single scalar value. Our experiments on colon tissue images reveal that this new object definition and characterization provides distinguishing representation of normal and cancerous histopathological images, which is effective to obtain more accurate classification results compared to its counterparts.

Keywords: Histopathological image representation, digital pathology, automated cancer diagnosis, tissue decomposition model, blob.

ÖZET

HİSTOPATOLOJİK GÖRÜNTÜ TEMSİLİ VE SINIFLANDIRMASI İÇİN İKİ KATMANLI DOKU AYRIŞTIRMA MODELİ

Tunç Gültekin
Bilgisayar Mühendisliği, Yüksek Lisans
Tez Yöneticisi: Doç. Dr. Çiğdem Gündüz Demir
Nisan, 2014

Sayısal patolojide, etkin görüntü temsili tasarımı, gürbüz otomatik tanı sistemlerinin geliştirilmesi için çok önemlidir. Histopatolojik görüntüler tipik olarak piksel seviyesinde kayda değer gürültü içerebilmektedir. Bundan dolayı, birçok çalışma, pikselleri doğrudan kullanmak yerine, nesne tabanlı gösterimlerin geliştirilmesini önermiştir. Bu önceki çalışmalar, çoğunlukla, görüntüdeki histolojik doku bileşenlerini yaklaşık temsil edecek şekilde renk bilgisini temel alan nesneler tanımlar ve tanımlanan bu nesnelerin uzamsal dağılımını görüntü temsili ve sınıflandırması için kullanır. Bu nedenle, nesne tanımlamasının, görüntü temsilinde doğrudan etkisi vardır, dolayısıyla da sınıflandırma doğruluğunu etkilemektedir. Bu tezde, histopatolojik görüntülerin etkin temsili ve sınıflandırması için yeni bir model sunmaktayız. Bu modelin iki tane katkısı bulunmaktadır. İlk olarak; görüntüler üzerinde çok tipli nesnelerin tanımlanması için, iki katmanlı yeni bir doku ayrıştırma yöntemi sunmaktadır. Önceki çalışmalardan farklı olarak, nesneler; desen, şekil ve boyut bilgileri birleştirilerek tanımlanır ve elde edilen bu nesneler, tek bir histolojik bileşene ya da farklı özellikteki doku alt bölgelerie karşılık gelebilir. İkinci katkı olarak, sunduğumuz bu yeni model, verilen nesnenin şekil ve boyutunu tek bir skalar değer olarak karakterize etmek için, baskın blob ölçeği adını verdiğimiz yeni bir metrik tanımlar. Kolon doku görüntüleri üzerinde yaptığımız deneyler, bu yeni nesne tanımlaması ve karakterizasyonunun, normal ve kanserli histopatolojik görüntülerinin ayırt edici bir temsiline olanak verdiğini ortaya koymaktadır. Bu ise, önceki çalışmalara göre, daha yüksek doğrulukta sınıflandırma sonuçlarının elde edilmesinde etkindir.

Anahtar sözcükler: Histopatolojik görüntü temsili, sayısal patoloji, otomatik kanser tanısı, doku ayrıştırma modeli, blob.

Acknowledgement

I would like to thank my advisor Assoc. Prof. Dr. Çiğdem Gündüz Demir. Without her guidance and support, I would not finish this thesis. I am also grateful to my jury members Assoc. Prof. Dr. Selim Aksoy and Prof. Dr. Billur Barshan for their time reading and evaluating this thesis.

I owe my deepest gratitude to my mother Nurhal Gültekin, my brother Burç Gültekin and my fiance Beril Kavaklı. This thesis would not be possible without their support, patience and love.

I thank my friends especially Can, Sitar, Shatlyk and Şerif for their help and moral support during my study. Special thanks go to Salim and Dilara for their endless support, I did not feel alone through their friendship and I am very lucky to have such great friends.

Lastly, I would like to thank to The Scientific and Technological Research Council of Turkey (TÜBİTAK) for providing financial assistance during my study, through the BİDEB 2210 domestic scholarship for graduate studies program and project 110E232.

Contents

List of Figures

List of Tables

Chapter 1

Introduction

Different tissues come together to form an organ in the body. Depending on its type, cancer causes different kinds of changes in these tissues. Thus, in cancer diagnosis and grading, pathologists examine the tissue changes considering the tissue type and may attach different levels of importance to the changes occurred in different tissue regions. For example, colon contains epithelial and connective tissues. In the diagnosis of colon adenocarcinoma, which accounts for 90-95 percent of all colorectal cancers [1], examining epithelial tissue regions is more important since this cancer type originates from the epithelial tissue and causes substantial changes in these regions (Fig. 1.1). In this work, we focus on a new tissue decomposition method for histopathological image characterization and classification.

1.1 Motivation

In the digital pathology literature, classification studies extract mathematical features to model the tissue changes and use them to classify histopathological images. The previous studies have used two main approaches for feature extraction. In the first approach, they extract features for each image pixel using various

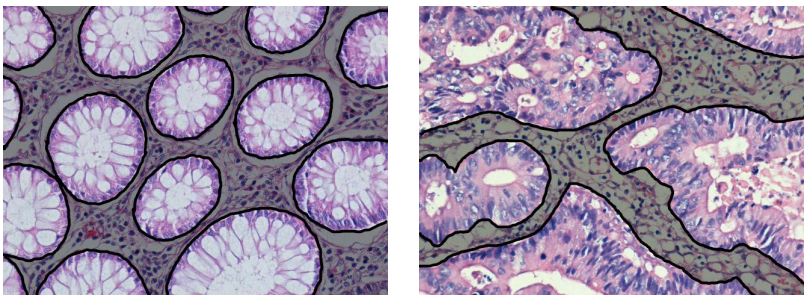

(a) (b)

Figure 1.1: (a) A normal and (b) a cancerous colon tissue image. On these images, epithelial (non-shaded) and connective (gray-shaded) tissue regions are shown.

methods including intensity histograms [2, 3], co-occurrence matrices [4, 5], filters [6, 7], and local binary patterns [8, 9]. They then define global features accumulating the pixels' features over an entire image. However, the image may contain local regions corresponding to different tissue types, which may show different image characteristics. Thus, globally accumulating the pixels' features without considering the local regions may weaken the representative power of these features and may lead to misclassifications. In addition to this, the extracted features consist of only textural information; however cancer may also cause structural deformations in the tissue. Susceptibility to pixel level noise is another issue of these kinds of studies. Since the features are directly extracted from image pixels, noise over pixels may negatively affect the classification accuracies.

In the second approach, the studies define objects in an image to represent histological tissue components and work on these objects instead of image pixels. The majority of these studies define objects for nucleus components and characterize the image with global features extracted from a graph of these components [10, 11, 12]. In recent studies, multi-typed objects are also defined for representing stromal and luminal components, and their spatial distributions are quantified using graphs [13, 14] as well as defining object textures [15]. These studies suffer less from pixel level noise and they may utilize both structural and textural information. However, they define objects over an entire image similar to the first approach and characterize the image without making any distinction

between the objects defined in the local regions of different characteristics.

1.2 Contribution

In this work, we propose a new two-tier tissue decomposition method for histopathological image characterization and classification. In the first tier of this method, we decompose an image into a set of local regions (objects) that show similar texture characteristics. Then, in its second tier, we put these regions into further categories based on their shape and size properties that we quantify by introducing a new metric. Finally, we construct a graph on the regions and use its edge distribution for image representation and classification.

The main contributions of this thesis are twofold. First, it proposes a new decomposition method for defining its objects (local regions). Different than the previous studies that defined nucleus locations as their objects, it identifies multi-typed objects and uses their distribution for tissue quantification. The proposed model is also different than the recent studies, which also used multi-typed objects, in the sense of defining the objects. In the previous works [13, 14, 15], objects are defined by locating circles of various radii on the dominant colors (white, pink, and purple) of histopathological images stained with hematoxylin-and-eosin. Since different tissues (e.g., epithelial and connective tissues shown in Fig. 1) have similar color distributions, there is no distinction between the types of the circular objects defined on the local regions of different tissue types. On the other hand, the decomposition method proposed by this thesis uses texture to identify objects in its first tier. Since texture is more distinctive than color for these local regions, the objects are expected to show more variety among the local regions of different tissue types. This helps better represent histopathological images and more accurately classify them. Additionally, previous works restrict objects to have regular shapes (simply circles). On the other hand, our new decomposition method does not have such kind of restriction and allows us to define irregular-shaped objects that directly correspond to histological tissue components (e.g., cell nuclei) or approximately represent local subregions of

different characteristics (e.g., epithelial cell regions). Since the second tier of the proposed method further categorizes these irregular-shaped objects based on their shape and size, it is expected to define more distinguishing objects for tissue image representation.

As its second contribution, this thesis introduces a new metric, which we call "dominant blob scale", to quantify the shape and size of the irregular-shaped objects. To this end, it defines a set of ring-like filters with different sizes, iteratively convolves each object with these filters, and quantifies the object with the size of the filter that covers this object. This metric uses the idea of blob definition, which is frequently employed in different computer vision applications such as salient point localization [16, 17, 18] and object tracking [19, 20]. Blobs are also used for feature extraction; previous studies [21, 22, 23] use blobs to define closed areas from which features will be extracted. On the other hand, different than these previous studies, our current work directly uses blobs (their scales) in an iterative algorithm to define a feature that quantifies the size and shape of an irregular-shaped object with a single scalar value.

Working on 3236 microscopic images of colon tissues, our experiments demonstrate that the distribution of the multi-typed objects, defined and categorized by our new decomposition method, is more effective in histopathological image representation and gives more accurate results in classification compared to its counterparts.

1.3 Outline

The outline of the thesis as follows. In Chapter 2, we first give the background about histopathological tissue image classification and then mention the existing approaches. In Chapter 3, we describe our two tier tissue decomposition method in detail. In Chapter 4, we explain the dataset, the methods that we used for comparison and the procedure of parameter selection and evaluation. Finally, in Chapter 5, we present conclusions and future aspects of our study.

Chapter 2

Background

In this chapter, we firstly give a brief background information about colon adenocarcinoma on which we conduct our experiments and how it deforms the organization in colon tissues. Then, we explain the pixel-based and object-based methods, developed for automated cancer diagnosis and the literature of blob detection.

2.1 Domain Description

The adenocarcinoma is an abnormal mass of epithelial tissues which have glandular characteristics and it arises as a result of abnormal cell division or growth. This type of cancer is seen in different parts of the human body such as lung, colon, prostate, and pancreas. In this study, we concentrated on automated diagnosis of the colon adenocarcinoma, which accounts for 90-95 percent of all colorectal cancers.

Colon glands are comprised of water absorbing columnar epithelial cells and mucus secreting goblet cells, which are illustrated in Fig. 2.1. Absorbed water is given to blood and secreted mucus is utilized for lubrication of the dehydrated feces. It prevents colon being damaged by easing passing of feces. The colon

adenocarcinoma affects these glandular and epithelial tissues and prevents doing their work by deforming their structures. Although the colon adenocarcinoma is fatal when it spreads, it can be curable with early diagnosis. Pathologists benefit the results of biopsy techniques for diagnosis. To do so, small samples are taken from colon tissues and these samples are fixed, dissected and stained. Staining unveils different parts of tissues by marking them with the different colors and eases to differentiate them from each other. For instance, hematoxylin&eosin technique, stains nuclei with blue-purple, stromas with pink whereas luminals remain unstained. The main histological components of a tissue are illustrated in Fig. 2.3

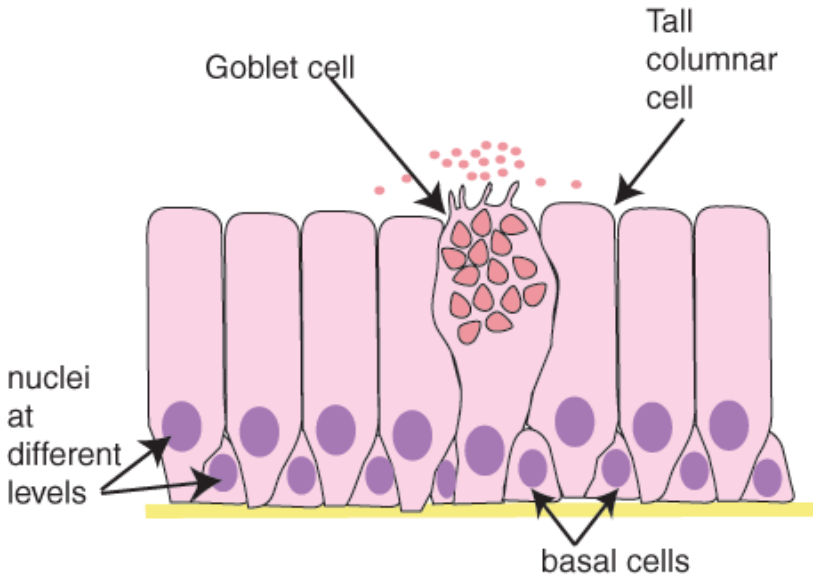

Figure 2.1: Goblet and columnar epithelial cells.[1]

Stained biopsy samples are examined and classified according to the deformations in the distribution of histological components. In this study we focus on three classes in the context of adenocarcinoma classification. These classes are normal, low grade cancerous, and high grade cancerous. Normal tissues, which do not contain any cancerous regions and do not reveal any deformations in its components' distributions and appearances. Examples of normal tissues are shown in Fig. 2.3(a)-(c). Cancer causes deformations in these appearances and the distribution. Since the colon adenocarcinoma originates from epithelial cells, which

[1]The image is taken from; www.histology.leeds.ac.uk/tissue_types/epithelia/assets/goblet1.gif

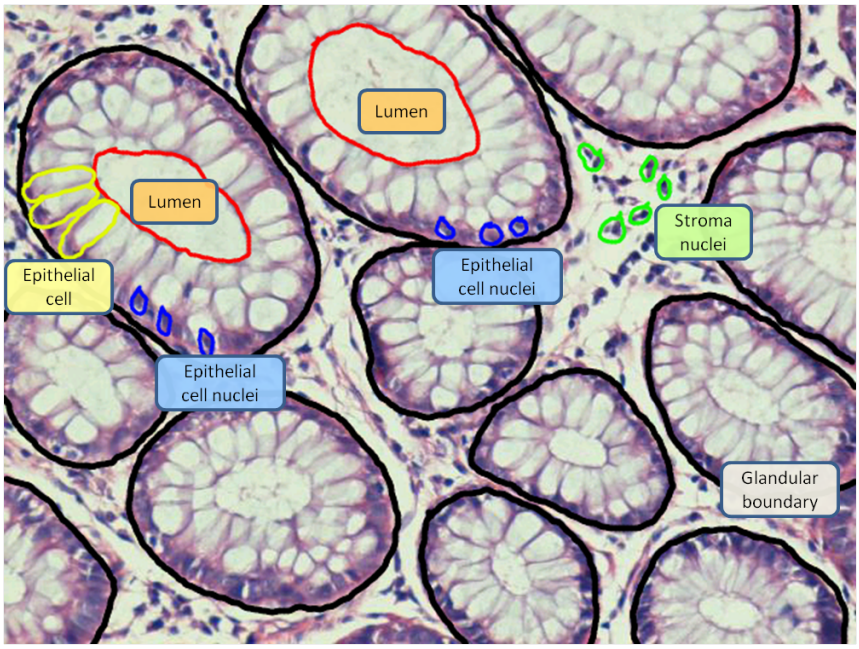

Figure 2.2: Histological components in a colon tissue.

form glands in a colon tissue, it causes deformations in the structure of glands. In low grade cancer, this deformation is low and gland structures are still distinguishable. In the late stages of the adenocarcinoma; low grade cancerous regions turn into high grade regions so that their shapes and textures of the glands are excessively changed. It is hard to differentiate the glands. Low grade and high grade tissue examples are shown in Fig. 2.3(d)-(f) and Fig. 2.3(g)-(i) respectively.

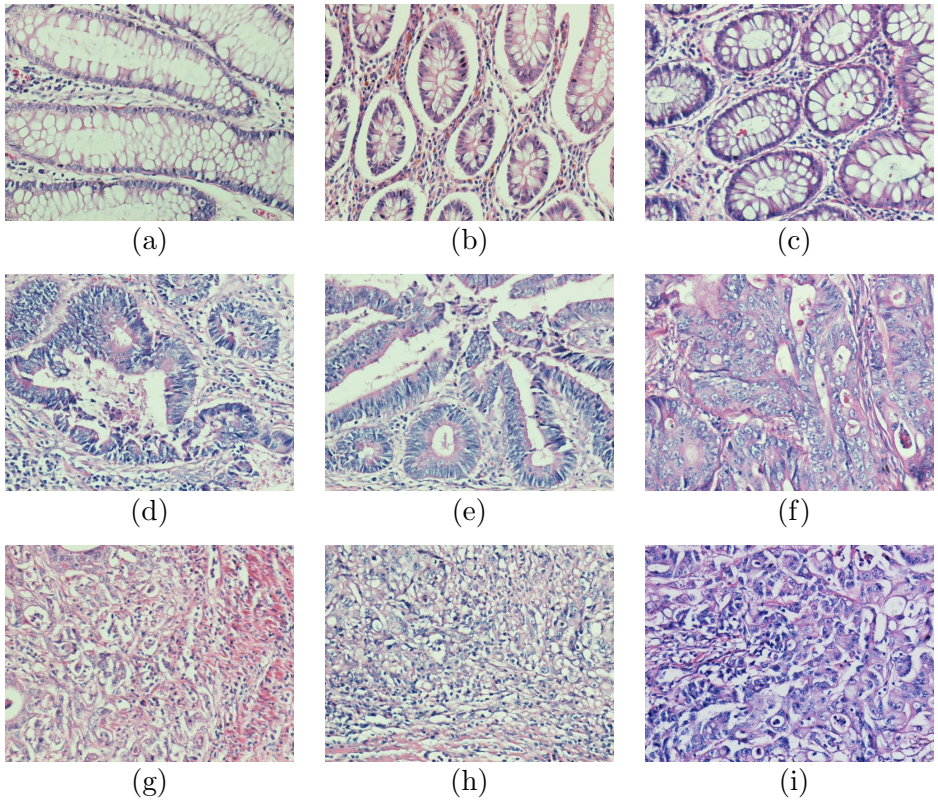

Figure 2.3: Examples of tissue classes considered in this thesis: (a)-(c) normal tissues, (d)-(f) low grade adenocarcinomous tissues, (g)-(i) high grade adenocarcinomous tissues.

2.2 Automated Cancer Diagnosis

In this sub-section we explain the existing techniques developed for automated cancer diagnosis and tissue classification. These techniques can be grouped into 2 main categories: pixel-based methods, and object based-methods.

2.2.1 Pixel Based Methods

Pixel based methods use image pixels directly and quantify the first and second order statistics on intensity or color values. To do so, they utilize various approaches such as, intensity histograms, co-occurrence matrices, filter banks, local binary patterns and fractal geometry.

2.2.1.1 Intensity Histograms

Intensity histograms are used for both gray-level and color images. For gray-level images, the intensity value of each pixel is quantized into N bins and the histograms are generated by calculating the frequency of each bin value. Either the values in these histograms or the statistics such as the mean, standard deviation, smoothness, skewness, uniformity, and entropy can be employed as features [24, 25]. For color images, the values of the color channels are quantized into bins independently and three different intensity histograms are obtained for an image. Likewise, the values in these histograms are directly used or the statistics are calculated on these values.

Intensity histograms are generated by accumulating all pixel intensities and they describe the entire images intensity distribution. However, tissue images may contain irrelevant regions for cancer diagnosis, for example non-glandular regions are not so important in colon adenocarcinoma diagnosis and considering these regions in the construction of the intensity histograms may lead to misclassifications. In addition to this adenocarninomas cause shape deformations in the histological tissue components but these deformations cannot be captured by

using intensity histograms since they only give information about intensity/color distribution.

2.2.1.2 Co-occurrence Matrices

Co-occurrence matrix features quantify the spatial relationship of quantized pixels' intensities. A co-occurrence matrix m_d is specified by relative frequencies of two pixels' values. Particularly, an entry $m_d[i, j]$ counts the number of occurrences of pairs of two pixels that have intensities of i and j and located at the distance of d and the orientation of θ with respect to each other [26, 27]. The size of a co-occurrence matrix depends on the number of quantization levels. It may be large and sparse thus, Haralick features [28], are usually computed. Definitions of Haralick features are shown in Table 2.1. In this table, μ_x and μ_y are the pixels' intensity means and σ_x and σ_y are the pixels' standard deviations.

Since co-occurrence matrices encode spatial distribution of pixels' intensities, they lead to better representations for tissue images than intensity histograms. However, similar to intensity histograms, they consider glandular and nonglandular regions together to define features, which may negatively affect classification performance.

$$
\begin{aligned}
\text{energy} &= \sum_i \sum_j M_d(i,j)^2 \\
\text{entropy} &= -\sum_i \sum_j M_d(i,j) \log M_d(i,j) \\
\text{contrast} &= \sum_i \sum_j (i-j)^2 M_d(i,j) \\
\text{homogeneity} &= \sum_i \sum_j \frac{M_d(i,j)}{1+|i-j|} \\
\text{correlation} &= \sum_i \sum_j \frac{(i-\mu_x)(j-\mu_y)M_d(i,j)}{\sigma_x \sigma_y} \\
\text{dissimilarity} &= \sum_i \sum_j |i-j| M_d(i,j) \\
\text{inverse difference moment} &= \sum_i \sum_j \frac{M_d(i,j)}{1+(i-j)^2} \\
\text{maximum probability} &= \max_{i,j} M_d(i,j)
\end{aligned}
$$

Table 2.1: Haralick features

2.2.1.3 Filter Banks

The human better senses some specific texture transitions including corners, edges, and the regions that have periodically changing intensity values. By using these basic cues, it recognizes scenes. Filter banks are convolutional kernels that mimic human visual perception. An example filter bank [29] is given in Fig. 2.4. When an image is convolved with filters, each convolution result corresponds to a basic textural transition and the features extracted from transitions usually better represent the image than the previous methods.

The extracted features can be defined by using first, second or high order statistics [30]. Additionally raw outputs can be used after applying dimensionality reduction methods such as PCA and LDA [31]. There also exits some clustering strategies that group similar pixels having similar filter responses and generate their histograms of them for image classification [32, 33]. Although filter banks are effectively used for texture definition, it does not give any information about the distribution of histological tissue components, which may be useful cancer

diagnosis.

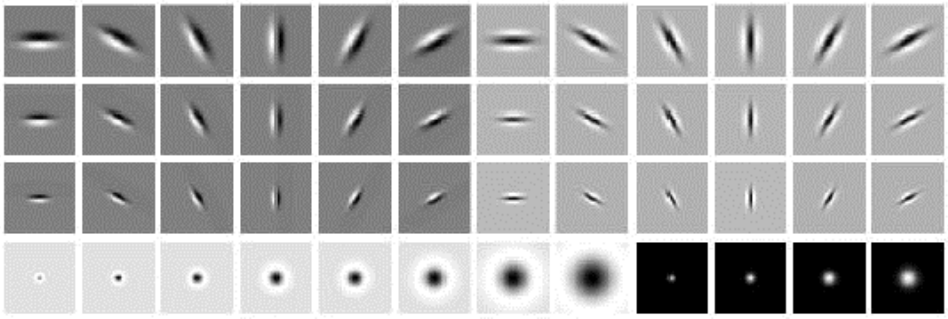

Figure 2.4: The Leung and Malik's filter bank has a mix of edge, bar and spot filters at multiple scales and orientations.

2.2.1.4 Local Binary Patterns

The local binary pattern describes a texture for a pixel p by quantifying the pixel values of its neighbors with a binary string [34]. To do so; the intensity of each of this image pixel is compared with those of its eight neighbors in a clockwise or counter-clockwise order. If the value of the compared pixel is greater than the value of pixel p, it is represented with 1 in the binary strings otherwise it is represented with 0. At the end, an eight bit binary string is obtained for each pixel and this string describes a rotational variant texture (Fig. 2.5). By shifting or grouping ones in the binary string, rotational invariant textures are obtained. Then its decimal equivalent is used as a feature for this pixel.

Then histogram of local binary patterns is used for various classification applications of computer vision [35] and medical image processing [36]. It is a powerful descriptor for texture classification. However, it is based on pixels, thus classification performance may reduce for the cases where irrelevant pixels also exist in the image; such as the pixels of non-glandular regions for adenocarcinoma classification.

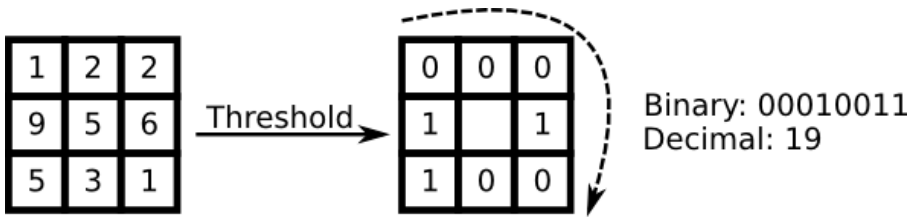

Figure 2.5: An example local binary pattern calculation.

2.2.1.5 Fractal Geometry

Fractals are mathematical shapes that repeat themselves in their lower scales. They may be exactly or nearly the same in different scales [37]. Fractals are distinguished from each other by the fractal dimension measure. It describes changing of space filling capacity of a pattern from bigger scales to smaller scales.

Fractals are observed in many different natural formations such as vegetables Fig. 2.6(a), snowflakes Fig. 2.6(b) and blood vessels Fig. 2.6(c). Many studies [38, 39] have used the fractal dimension measure. These studies generally use this measure in addition to other texture methods.

(a)

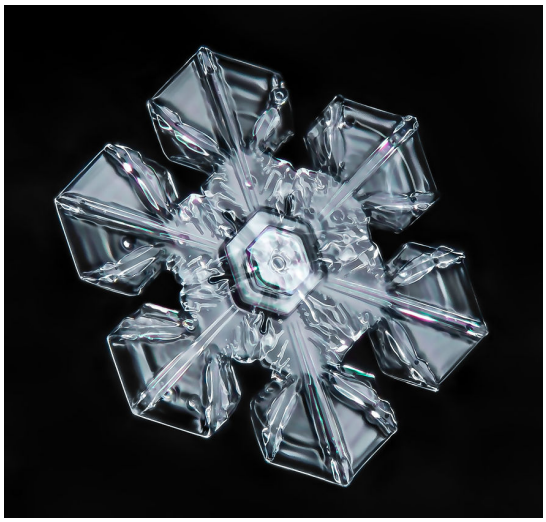

(b)

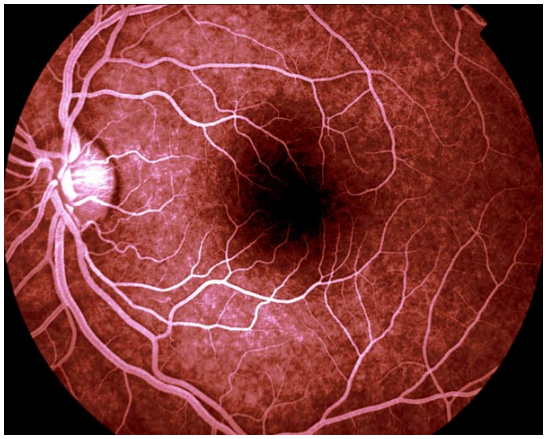

(c)

Figure 2.6: Examples of natural fractal formations; (a) is the broccoli plant, (b) is the snowflake, (c) is the eye retina vessels.

2.2.2 Object Based Methods

Object based methods define objects on histological tissue components by grouping pixels in an image and work on these objects instead of image pixels for classification. These methods usually characterize images with global features extracted from a graph of the defined objects. For graph construction, they used many different techniques such as; Delaunay triangulation, minimum spanning tree, and color graph. Additionally features can be extracted by defining textures on the objects.

2.2.2.1 Delaunay Triangulation Features

Delaunay triangulation method constructs a triangulation for a set of points in the plane. To this end, Delaunay triangulation maximizes the minimum angles of the triangles and It also satisfies the condition of the circumcircles of all triangles have empty interiors. Although, the constructed triangulation is not unique in case of there are four or more points on the same circle, it provides a nearly unique triangulation for a set of P points.

In histopathological image representation, there are many studies using Delaunay triangulation [10, 5]. In these studies; objects are usually defined on nuclear tissue components and a Delaunay triangulation is constructed by using centroids of the objects. Afterwards, the statistical features are extracted from triangles and their edges. The extracted features give information about structural deformation in tissues but they do not encode textural information.

2.2.2.2 Minimum Spanning Tree Features

The minimum spanning tree of a graph is a sub-graph of that connects graph all nodes without having any circle. A graph may have many different spanning trees. In weighted graphs, minimum spanning trees correspond to the sub-graphs which have minimum edge length summations. An example minimum spanning tree of a weighted graph is shown in Fig. 2.7.

In medical image classification, minimum spanning trees are used for feature extraction [40, 41, 7]. Similar to the Delaunay triangulation approach, these studies define objects over an entire image and construct a graph on these objects. Subsequently, they generate the minimum spanning tree of that graph and calculate features such as; mean, standard deviation, and disorder of the edge lengths.

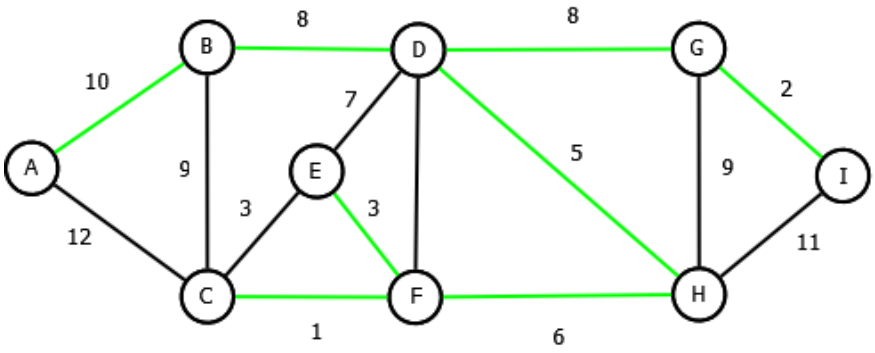

Figure 2.7: An example minimum spanning tree (green edges) of a weighted graph.

2.2.2.3 Color Graph Features

Object based methods generally define objects only on nuclear components of tissues. However, deformations caused by cancer occur in stromal and luminal regions as well. For that the Color graph method define [13]. In this method, a graph is created with Delaunay triangulation by considering nuclear, stromal, and luminal objects as nodes. Subsequently, edges of the graph are colored according to their end-object types and features are extracted from the colored edges.

These features include the colored versions of the average degree, average clustering coefficient and diameter. Despite the fact that color graphs better model histopathological tissues than the previous approaches [41], it does not provide textural information, which is useful for tissue classification.

2.2.2.4 Object Texture Features

Modeling different histological tissue components, can improve classification performance. In addition to this relative organizations of these components are important. To benefit from the relative organizations of objects, object texture approach was proposed [15]. In this approach, textures are modeled with binary strings as similar to local binary patterns [34]. However as opposed to local binary patterns in this texture definition, binary strings are generated from nuclear, stromal and luminal objects' neighborhoods instead of pixels. To this end, spatial organizations of histological tissue objects are encoded and they correspond to object-level textures. Histograms of the encoded object textures are used as features for histopathological tissue classification.

2.3 Blob Detection

Blobs are image regions, whose pixels have the same or nearly same color and transparency properties. For this reason, they differ from their surrounding regions. Blobs are employed in many different application areas of computer vision. Salient point localization [16, 17, 18] and object tracking [19, 20] are examples of them. Blobs are also used for feature extraction; previous studies [21, 22, 23] use blobs to define image regions for extracting features. Different than these, in this thesis, we make use of blobs' scales in an iterative algorithm directly to extract the features.

To localize blobs, the derivatives of functions are generally used as convolution kernels. These kernels should have a positive valued circular region at its center and a negative valued ring surrounding this positive region or vice-versa. When an image is convolved with this kind of kernel, image regions which have blobs produce high responses. By changing the size of the kernel, different sized blobs can be detected. The most common convolution kernels for blob detection are as follows;

2.3.1 Laplacian of Gaussian (LoG)

The size of a detected blob depends on the σ value, which is the standard deviation of a Gaussian. Convolution kernel is calculated as follows

$$g_\sigma = \frac{1}{\sqrt{2\pi\sigma^2}} exp\left(-\frac{x^2+y^2}{2\sigma^2}\right)$$

$$L_\sigma(x,y) = \nabla^2 g_\sigma(x,y) = \frac{\partial^2 g_\sigma(x,y)}{\partial x^2} + \frac{\partial^2 g_\sigma(x,y)}{\partial y^2}$$

$$LoG_\sigma(x,y) = L_{xx} + L_{yy}$$

$$LoG_\sigma(x,y) = -\frac{1}{\pi\sigma^4}[1 - \frac{x^2+y^2}{2\sigma^2}]e^{\frac{x^2+y^2}{2\sigma^2}}$$

The Laplacian of a Gaussian can also be obtained by using a square matrix of the second order partial derivatives of a function, which is, Hessian matrix. The

trace TR of a Hessian matrix $H(x)$ equals to the Laplacian of a Gaussian [42]. A 2-dimensional LOG kernel is illustrated in Fig. 2.8.

$$H(x) = \begin{bmatrix} L_{xx} & L_{xy} \\ L_{xy} & L_{yy} \end{bmatrix}$$

$$LoG_\sigma(x, y) = TR(H) = L_{xx} + L_{yy}$$

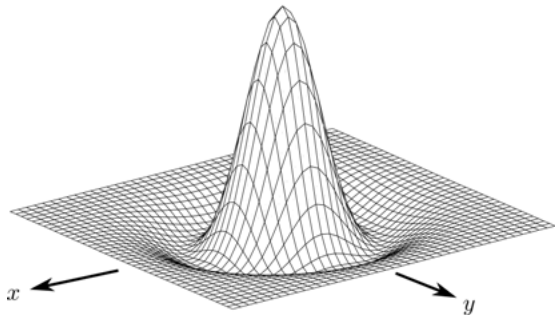

Figure 2.8: An illustration of a 2-dimensional LoG kernel.[2]

2.3.2 Difference of Gaussians (DoG)

It is a LoG approximation [17] and provides more efficient calculation since it does not require differentiation.

$$LoG_\sigma(x, y) \cong DoG_\sigma(x, y) = g_{\sigma_1}(x, y) - g_{\sigma_2}(x, y)$$

The best approximation occurs when

$$\sigma_1 = \frac{\sigma}{\sqrt{2}}\sigma_2 = \sqrt{2}\sigma$$

The difference of two 1-dimensional Gaussians is shown in Fig. 2.9.

[2]The image is taken from; miac.unibas.ch/SIP/07-Segmentation-media/figs/LoG.png

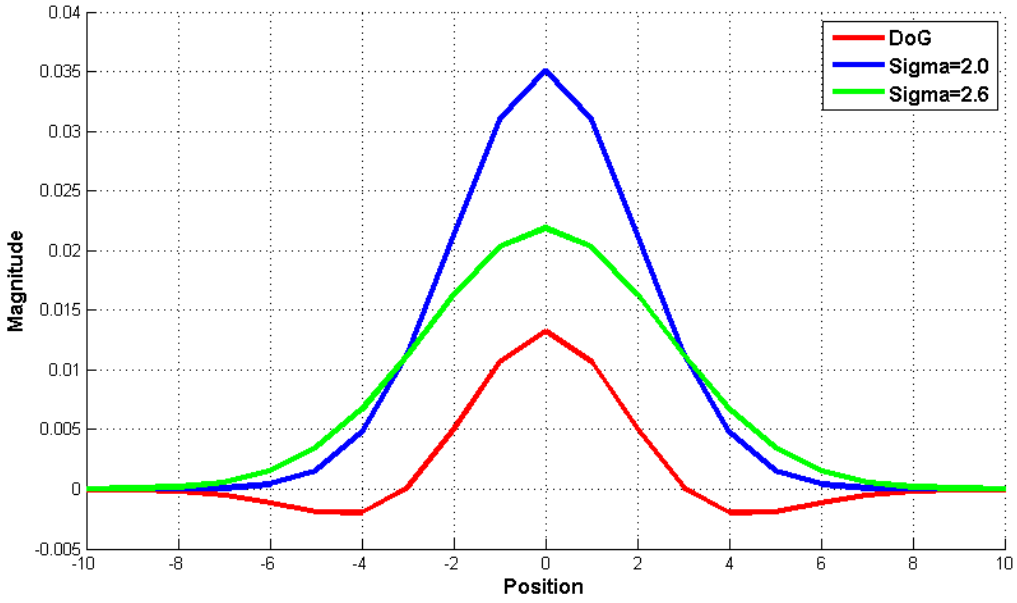

Figure 2.9: Difference of two 1-dimensional Gaussians.

Chapter 3

Methodology

The proposed model relies on decomposing a histopathological image into characterized objects and using the spatial relations among these characterized objects in the representation and classification of the image. In this model, we propose a new two-tier method for image decomposition. The first tier of this method locates objects on an image and pre-categorizes them based on their texture characteristics. Then, its second tier further categorizes the objects based on their shapes and sizes, which we quantify by introducing the *dominant blob scale* metric. An illustration of proposed decomposition method is given in Fig. 3.1. This decomposition method and the image representation and classification procedures are further detailed in the following sections.

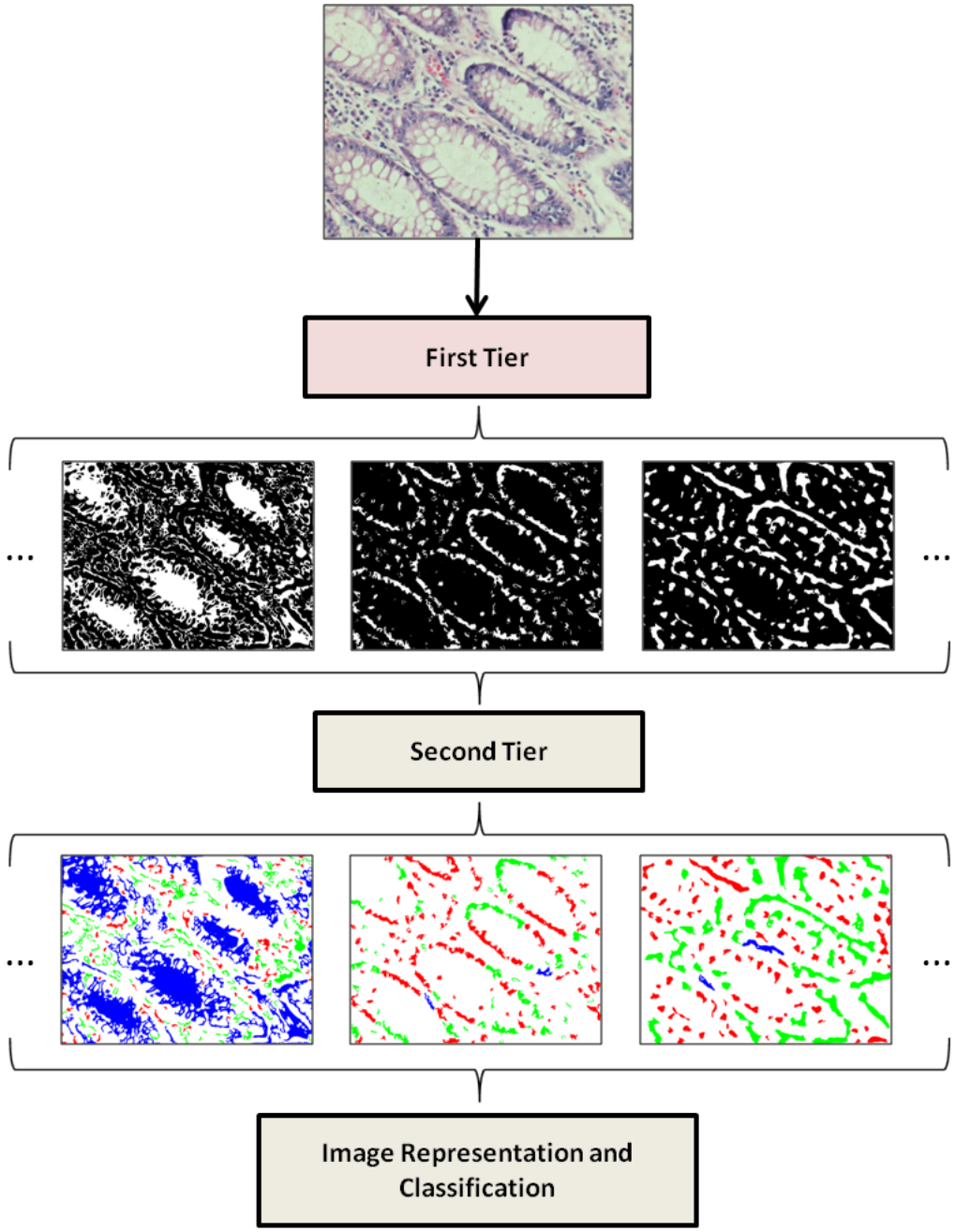

Figure 3.1: An illustration of the proposed decomposition method. Outputs of the first tier mostly represent different tissue objects such as lumen, nuclei, and epithelial cytoplasms whereas second tier's outputs correspond to the further categorized objects based on their `dbs` values. Red, green, and blue colors represent small, medium, and large objects categorized based on their `dbs` values.

3.1 Tissue Decomposition

We decompose an image I into the characterized objects using a two-tier method. In the first tier, we make use of texture characteristics. To this end, we convolve the normalized gray intensities of image pixels with the filters defined in the Schmid's filter bank [43]. These filters are illustrated in Fig. 3.2.

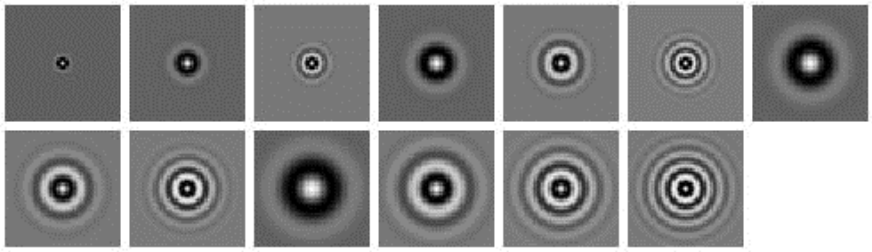

Figure 3.2: The Schmid's filter bank includes 13 rotationally invariant Gabor-like filters.

We then assign each pixel to one of the K clusters, learned by the k-means algorithm[1], according to the pixel's filter responses. At the end, we find connected components on the pixels of each cluster and take the components whose areas are greater than an area threshold T_{area} as image objects. These objects may correspond to individual histological tissue components or local regions of different tissue characteristics. For instance, Fig. 3.3 visualizes two different types of objects defined for an example image. As shown in this image, red objects mostly represent individual stromal cell nuclei whereas blue objects mostly correspond to epithelial cell nucleus regions. At the end of the first tier, we identify a set of image objects $\mathcal{O}(I) = \{o_i\}$, each of which is represented by its coordinates (x_i, y_i), its area a_i, and its cluster (pre-category) $\alpha_i \in \{1, ..., K\}$.

Note that this filter response labeling approach is different that its counterparts [32, 33]. It groups the same labeled pixels, finds their connected components, and uses the distribution of these connected components instead of using

[1]In our experiments, we randomly selected 20 images from each class and run the k-means algorithm on the pixels of these images.

the pixel distribution. Additionally, it only captures the tissue component level information, and thus eliminates pixel level noise.

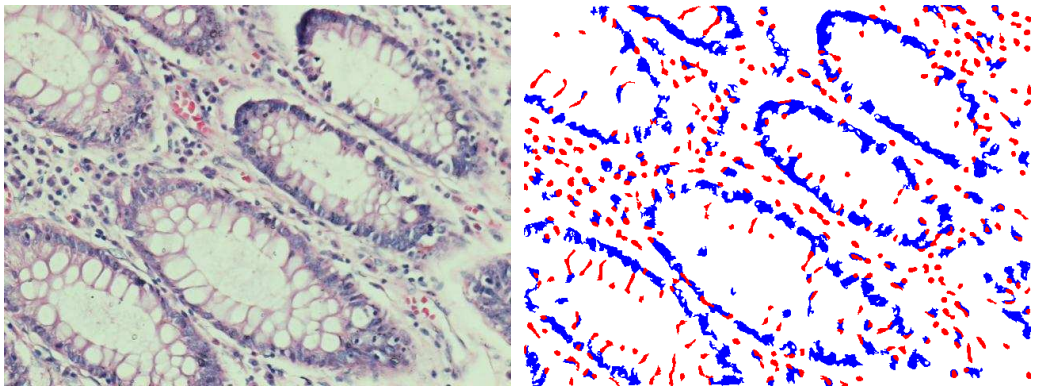

(a) (b)

Figure 3.3: (a) A normal colon tissue image and (b) two different types of objects defined for this image. Here red objects mostly represent individual stromal cell nuclei whereas blue objects mostly correspond to epithelial cell nucleus regions. Note that for better visualization of these two types, objects belonging to the other types are not shown in this figure.

In the second tier, for each object o_i, we compute the dominant blob scale metric (`dbs`), whose calculation details will be given in the next subsection. This metric is a continuous integer valued function that we propose to quantify the object's shape and size with a single value. In this thesis, we use this metric to group objects belonging to the same pre-category α_i into subcategories. For this purpose, we quantize the `dbs` of objects located on training images by the k-means algorithm and learn three clustering vectors corresponding to small, medium, and large scaled objects. Then, we compute the discretized `dbs` of an object, $\beta_i \in \{small, medium, large\}$, by assigning this object into one of these clusters. The `dbs` histogram of all training set objects, computed before quantization is shown in Fig. 3.4. We eliminate the objects whose area is lower than a threshold T_{area} for noise elimination. Note that when we learn clustering vectors corresponding to small, medium, and large categories, we do not consider the eliminated objects. Thus, these categories depend on the selected area threshold, which will be automatically selected by cross validation. For different values

of the object threshold, the intervals for defining these categories are given in Table 3.1. In this thesis, we employ a relatively simple method to define the subcategories using the `dbs` metric. However, it is also possible to design different methods that use this metric differently; investigation of these uses could be considered as a possible future work. The flowchart of the tissue decomposition procedure is given in Fig. 3.5.

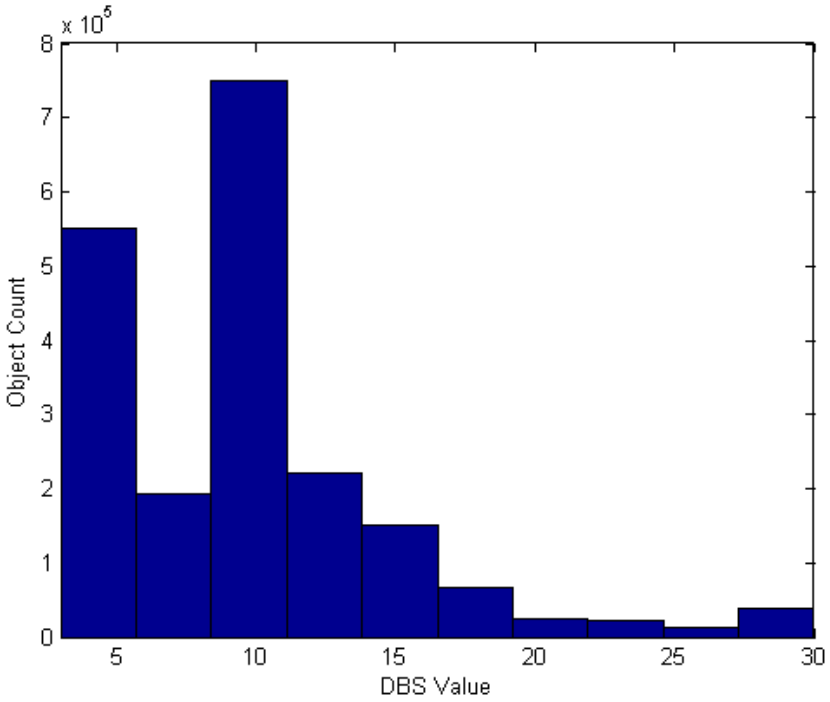

Figure 3.4: The `dbs` histogram of training set objects.

Table 3.1: For different object area thresholds, the `dbs` quantization intervals calculated on the training images.

T_{area}	Small	Medium	Large
20	dbs ≤ 6	$7 \leq$ dbs ≤ 15	$16 \leq$ dbs
30	dbs ≤ 6	$7 \leq$ dbs ≤ 16	$17 \leq$ dbs
40	dbs ≤ 7	$8 \leq$ dbs ≤ 17	$18 \leq$ dbs
50	dbs ≤ 7	$8 \leq$ dbs ≤ 18	$19 \leq$ dbs
60	dbs ≤ 7	$8 \leq$ dbs ≤ 18	$19 \leq$ dbs

After identifying the subcategories, we label each object with respect to its pre-category α_i and its discretized `dbs` β_i. In particular, we label the object o_i with a type $t_i = \gamma_{kj}$ if $\alpha_i = k$ and $\beta_i = j$. Thus, each object is labeled with one of the $3K$ different types.

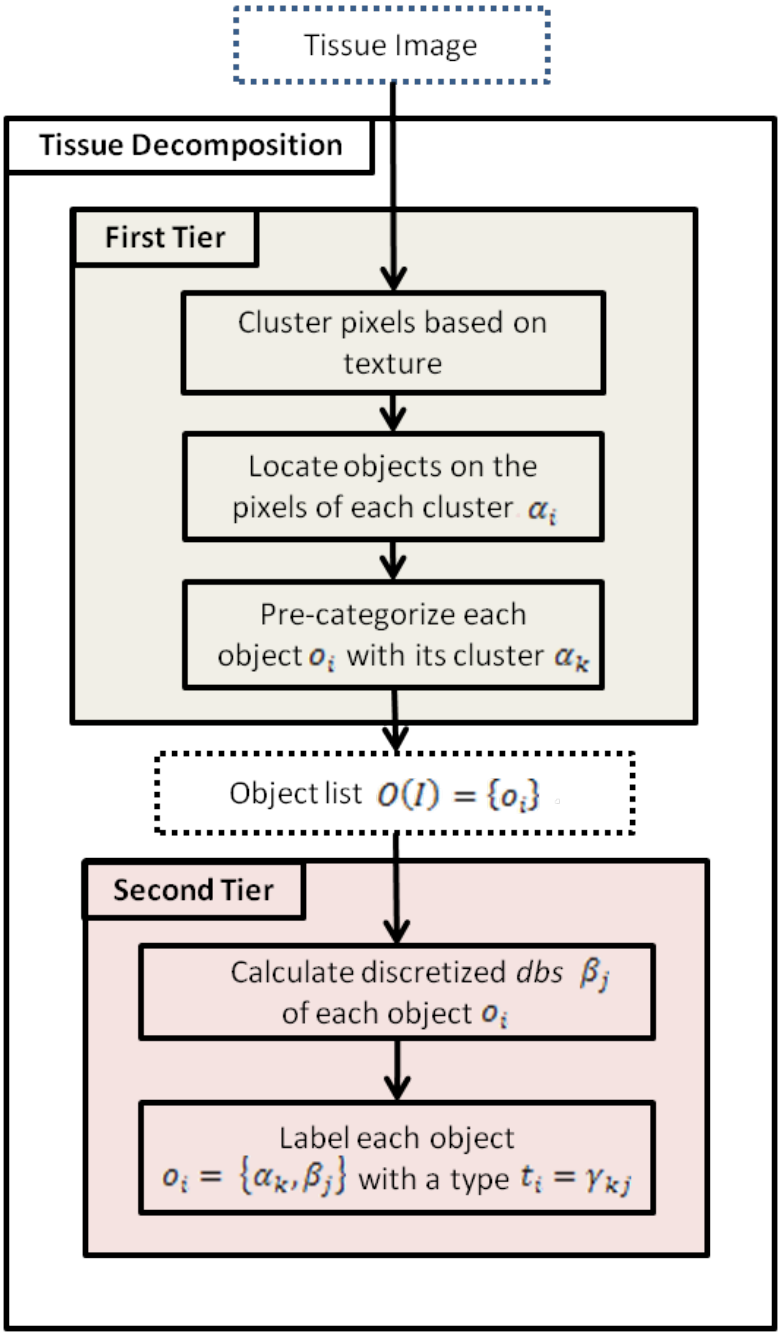

Figure 3.5: Flowchart for tissue decomposition.

3.1.1 Dominant Blob Scale

To calculate the `dbs` of a given object o_i, we iteratively convolve the binary representation of this object, where the pixels belonging to o_i are marked as 1 and all others as 0, with a set of ring-like filters (see Fig. 3.6) of different sizes. Then, we define $\texttt{dbs}(o_i)$ as the size of the filter that first covers the object o_i according to Definition 1.

Definition 1. An object o_i is said to be covered by a filter f_r with respect to a constant c_{pixel} if and only if c_{pixel} percent of its pixels are covered by f_r with respect to Definition 2.

Definition 2. A pixel p is said to be covered by a filter f_r if and only if the filter response for p is greater than 0.5.

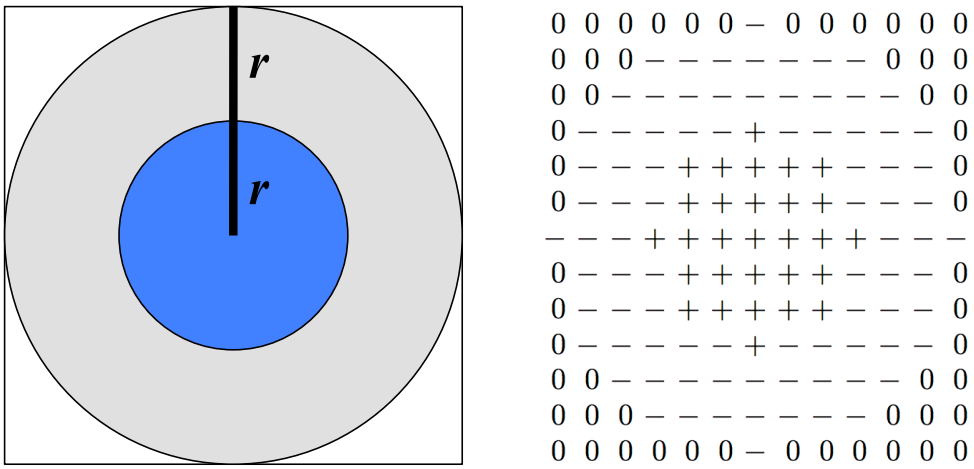

Figure 3.6: The ring-like filter f_r defined for the size r.

The pseudocode for the dominant blob scale calculation is given in Algorithm 1. This algorithm takes three inputs: The first one is the object $o_i = (x_i, y_i, a_i, t_i)$, which is represented by its coordinates (x_i, y_i), its area a_i, and its type t_i (assigned using the pre-category α_i and the subcategory β_i). The second one is the minimum size r_0 of the filter from which iterations start. The last parameter is the constant c_{pixel} used in Definition 1. Then, the algorithm outputs the dominant blob scale of the input object, $\texttt{dbs}(o_i)$, which is used to calculate the object's discretized `dbs` β_i, and hence its type t_i.

Algorithm 1 DOMINANT BLOB SCALE CALCULATION

Input: object o_i, smallest filter size r_0, constant c_{pixel}

Output: dominant blob scale `dbs` of the object o_i

```
1: r = r_0
2: area = 0
3: while area < c_pixel · a_i do
4:     f_r ← CreateFilter(r)
5:     g_i ← o_i * f_r
6:     area = 0
7:     for all pixels p of o_i do
8:         if g_i(p) > 0.5 then
9:             area = area + 1
10:        end if
11:    end for
12:    r = r + 1
13: end while
14: dbs = r − 1
```

In this thesis, we create a filter f_r with a size of r as follows. The filter includes a positive disk with a radius of r at its center and a negative ring with a width of r surrounding this disk. In this filter, we assign a positive value u_p to every entry in the disk such that their sum will be 1. Likewise, we assign a negative value u_n to every entry in the ring such that their sum will be -1. The iterative `dbs` calculation algorithm, which uses these filters, start covering object's pixels from its corners thanks to the existence of a positive disk surrounded by a negative ring. Thus, this algorithm yields larger `dbs` values for larger and rounder objects compared to smaller and more rectangular-like ones.

For objects of different sizes and shapes, Fig. 3.7 illustrates the responses of different sized-filters as well as indicates the one whose size r is used to define the `dbs` of these objects with cyan boundaries. The objects shown in the first four columns of this figure have exactly the same size but their shapes become

rounder from left to right. These objects are larger than those given in the last two columns of this figure. As shown in Fig. 3.7, rounder objects are covered by relatively large filters, leading to larger `dbs` values. Similarly, larger objects are covered by larger filters compared to smaller ones.

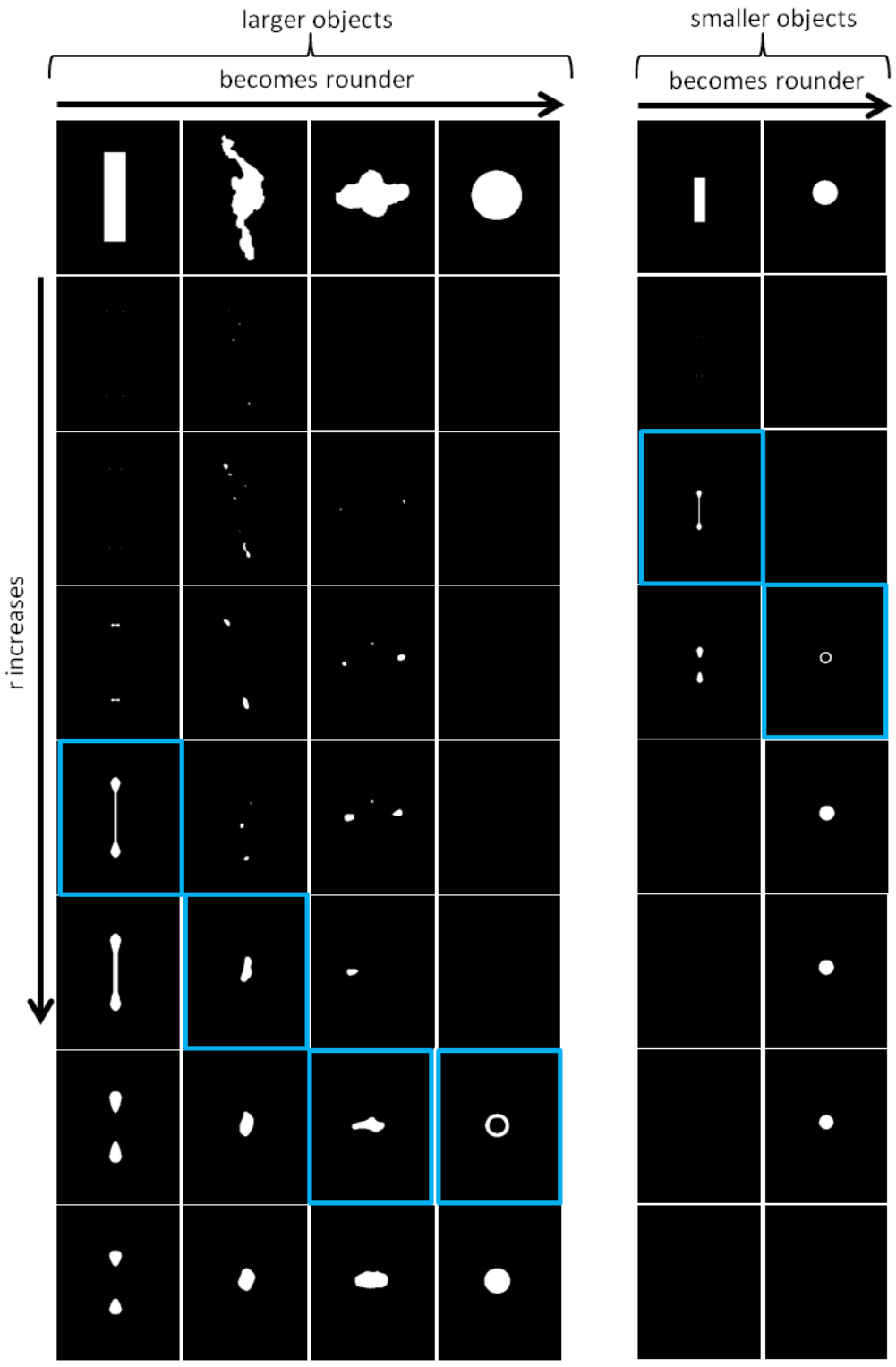

Figure 3.7: Illustration of `dbs` calculation for objects of different sizes and shapes.

The dominant blob scale calculation process includes a blob extraction stage. However, for blob extraction it makes use of ring filters as shown in Fig. 3.6 while traditional blob extraction methods [16] employ Laplacian of a Gaussian or a difference of two Gaussians as shown in Fig. 3.8. The reason behind our usage is that object representations are binary in our case. Thus, it is not necessary to use a Gaussian distribution in defining a filter kernel.

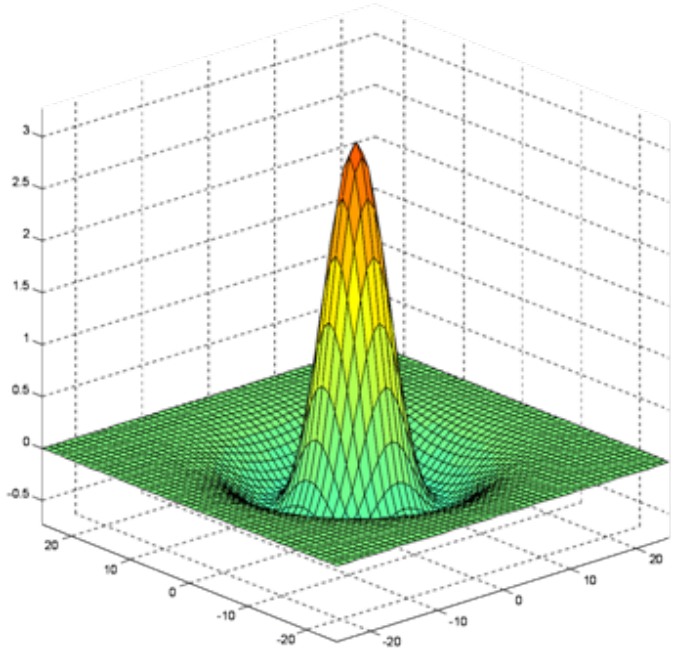

Figure 3.8: An example of a difference of two Gaussian's.

3.2 Image Representation and Classification

We characterize an image I by making use of the spatial distribution of its objects $\mathcal{O}(I) = \{o_i\}$. To this end, we construct a graph $G = (V, E)$ on the objects' centroids by Delaunay triangulation. In this graph, the vertex set V contains every object $o_i \in \mathcal{O}(I)$ and the edge set includes the triangle edges $e(o_u, o_v)$ that are labeled with respect to their end nodes. Particularly, we label the edge $e(o_u, o_v)$ with a type $\tau(t_u, t_v)$, where t_u and t_v denote the types of the objects o_u and o_v. Then, we use the distribution of edge types to represent the image I.

For instance, an example triangulation and the distribution of its edge types is illustrated in Fig. 3.9. Here for the sake of simplicity, only four node types are considered.

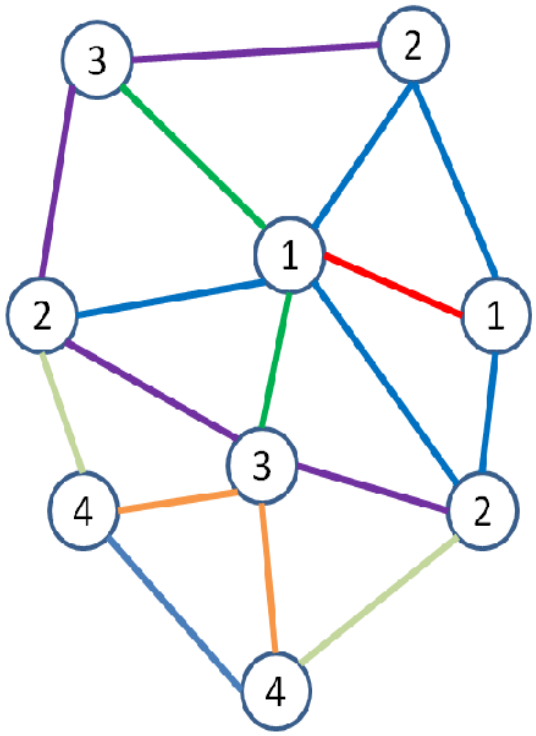

N1-N1	N1-N2	N1-N3	N1-N4
1	5	2	0

N2-N2	N2-N3	N2-N4
0	4	2

N3-N3	N3-N4
0	2

N4-N4
1

Figure 3.9: An example triangulation and the distribution of its edge types. Here numbers in nodes represent object labels.

In this representation, the dimension of a feature vector is $3K \cdot (3K+1)/2$ where K is the number of pre-categories (clusters) found in the first tier of tissue decomposition, since there exist $3K$ different types of objects. This dimension is usually high and may lead to curse-of-dimensionality. Thus, we automatically reduce the dimension on the training images. In particular, we eliminate an edge type τ from the representation if the number of edges of this type τ is smaller than an edge threshold T_{edge} for every image in the training set. Then, we use a support vector machine with a linear kernel for classification. The flowchart of the image representation and classification step is given in Fig. 3.10

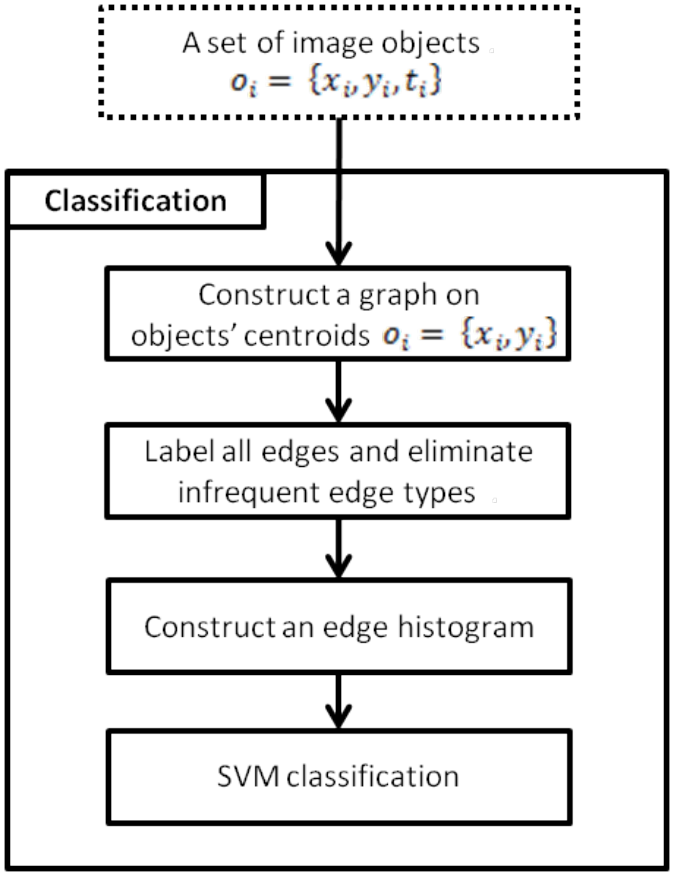

Figure 3.10: Flowchart for image representation and classification.

Chapter 4

Experiment Results

In this chapter, first we give information about the dataset that we conduct our experiments and explain the methods that we use for our comparisons. Subsequently, we describe our parameter selection procedure and present the results of our experiments. Finally, we discuss the effects of the parameter selection on classification accuracies.

4.1 Dataset

We conduct our experiments on 3236 microscopic images of hematoxylin-and-eosin stained colon tissues of 258 randomly selected patients. Images are obtained from the Pathology Department of Hacettepe University School of Medicine and taken using a Nikon Coolscope Digital Microscope with a 20× objective lens and at 640×480 pixel resolution.

We randomly divide these images into training and test sets such that they contain images of different patients. The training set contains 1644 images which are taken from the randomly selected half of the patients and the test set contains 1592 images taken from the rest of the images. We label the these images with

three different classes: normal, low-grade cancerous, and high-grade cancerous[1]. The training set contains 510 normal, 859 low-grade cancerous and 275 high-grade cancerous images of 129 patients. The test set contains 491 normal, 844 low-grade cancerous, and 257 high grade cancerous images of the remaining 129 patients.

4.2 Comparisons

To evaluate the performance of our proposed two-tier approach, we compare it with previous of the pixel based and object based methods. These methods are explained in sections 4.2.1 and 4.2.2 respectively. All these methods use SVMs with a linear kernel for their classification.

Furthermore, in order to understand the effectiveness of our two-tier model, we conduct some additional experiments. To this end, we make modifications in the steps of our model and analyze the effects of these modifications on the classification performance. These modifications are explained in Section 4.3.1

4.2.1 Pixel Based Methods

Pixel based methods extract features directly from image pixels. For the pixel based method comparison, we use five methods which extract their features using intensity histograms, co-occurrence matrices, Gabor filters, local binary patterns. In addition to extracting these features on entire images, we implement their grid-based variants. Since tissue images may contain irrelevant sub-regions for classification. To this end, we divide tissue images into fixed sized grids, extract features for each cell separately, and take the averages of all grid features to represent entire image. Besides we compare our results with the results of a previously implemented algorithm, called resampling based Markovian model (RMM), developed by our research group.

[1]The images are labeled by Prof. C. Sokmensuer, MD, who is specialized in colorectal carcinomas.

4.2.1.1 Intensity Histograms

For each image, we first quantize the gray-level intensities of the pixels into bins to reduce noise and then generate an intensity histogram of the quantized pixels. Next, we extract features by calculating the statistics of these features include the mean, standard deviation, kurtosis, and skewness. Additionally we implement its grid-based variant of to benefit from locality information by dividing images into fixed sized grids.

4.2.1.2 Co-occurrence Matrices

Similar to intensity histograms, we first quantize pixel intensities and then calculate the gray-level co-occurrence matrices of an entire image for eight different angular directions. After that, by taking the mean of these matrices we obtained rotational invariant co-occurrence matrix. For classification, we extract six features from the resulting co-occurrence matrix: energy, entropy, contrast, homogeneity, correlation and dissimilarity. For its grid-based variant, we divide an image into fixed sized grids, compute co-occurrence matrices for each grid entry and take the average of these matrices similar to the grid-based variant of the intensity histograms.

4.2.1.3 Gabor Filters

We convolve an image with log-Gabor filters in six orientations and four scales [44] to benefit from the advantages of filter responses which mimic human visual perception. Next, we take the averages of these responses and calculate their mean, standard deviation, minimum-to-maximum-ratio, and mode values as the features. Likewise, we also implement the grid-based variant of this technique.

4.2.1.4 Local Binary Patterns

To understand the performance of local texture descriptors, we compare the gray level intensity of each pixel with those of its eight neighboring pixels and generate a binary string for this pixel. In that binary string, the corresponding bit is 1 if the compared pixels intensity is greater than the intensity of that pixel; otherwise it is 0. By calculating the frequencies of the generated binary strings, we obtain features for classification. Here we did not implement a grid-based variant since it yields same feature values.

4.2.1.5 Resampling-based Markovian Model

For resampling-based Markovian model (RMM) [45] method, we first define random interest points on an image and then characterize each point using the pixels falling in window centered at this point. For characterization the histogram of quantized pixels and the J-value metric [46] are used. Then we use the sequence of these interest points in a Markov model for the classification of the image.

4.2.2 Object Based Methods

Object-based methods decompose a tissue image into objects and extract features from this object representation. For object-based method comparison, we make use of five different techniques: Delaunay triangulation, color graph, graph walk, hybrid model, and local object pattern approaches, which are explained in the following subsections.

4.2.2.1 Delaunay Triangulation

We construct a graph on nuclear components of a tissue image by using Delaunay triangulation. These components are purple circular objects of hematoxylin-and-eosin stained images. Afterwards, we extract features from the triangulation

graph including the average degree, average clustering coefficient, and diameter, as well as average, standard deviation, minimum-to-maximum ratio, and disorder of edge lengths and triangle areas.

4.2.2.2 Color Graph

As a colored version of the Delaunay triangulation method, we construct a graph on nuclear, stromal and luminal components of a tissue image. Subsequently, we color the edges of that graph according to their endpoint object types and extract features on the colored edges. These features include the colored versions of average degree, average clustering coefficient and diameter [13].

4.2.2.3 Graph Walk

The graph walk approach [47], represent a tissue image with a set of sub-graphs and classify them according to their edge distributions. These sub-graphs are generated by traversing the graph by the breadth-first search algorithm. Then, we vote the results of these sub-graph classifications to find the class of the entire image.

4.2.2.4 Hybrid Model

The Hybrid Model [14] uses graph similarities to detect interest regions and then generate features on these regions. For that it represents an image with an entire graph and defines small query graphs as the reference to normal gland structures. After that it searches these query graphs within the entire graph to find the interest regions. At the end, it classifies the image with the features defined on these regions. These features include graph edit distances as well as texture measures.

4.2.2.5 Local Object Patterns

As an object-based version of local binary patterns, the local object pattern [15] approach was proposed. This approach initially decomposes a tissue image into nuclear, stromal and luminal objects. After that it extracts binary strings from the distribution of neighboring objects and uses their histograms for classification. These binary strings correspond to different textural representations as in local binary patterns. However, in local object patterns, object types are used for comparison instead of gray-level intensities of the pixels.

4.2.3 Two-Tier Model Modifications

To understand the effects of each part of our two-tier model, on classification accuracies, we make some modifications on our approach and evaluate the modified versions independently. For investigation of the effectiveness of using an object-based representation, we define two methods: SchmidFilterBankResponses and QuantizedPixels methods. To understand the separate contributions of the first and second tiers, we evaluate each one's classification performance independently. Lastly, to find out the effectiveness of the `dbs` metric, we use another metric for further categorizing the objects in the second tier. Details of these variations are given in the following subsections.

4.2.3.1 *SchmidFilterBankResponses* Method

We convolve tissue a image with 13 different filters, that are defined in the Schmid's filter bank and obtain 13 dimensional responses for each pixel. Next, we take the average and standard deviation of the each of the 13 responses over all pixels. For image representation, we concatenate the average and standard deviation values. This operation produces a 26-dimensional feature vector for each image.

4.2.3.2 QuantizedPixels Method

For this method, we take the Schmid filter bank responses of the pixels and assign each pixel to one of K clusters, learned by the k-means algorithm as we did in the first-tier of our model. To define the cluster centroids, we randomly select 20 training images from each class and learn clustering vectors by running the k-means algorithm on the pixel responses of these training images. After that, we represent images with the bag-of-words representation of the labeled pixels.

4.2.3.3 OnlyFirstTier Method

To analyze the effects of the second tier of our proposed model, we remove it from the model and just use the characterized objects defined at the end of the first tier. Thus OnlyFirstTier method defines a graph on the objects and labels the graph edges with respect to the object types α_i defined by the first tier.

4.2.3.4 OnlySecondTier Method

We analyze the effects of the first tier by removing it from the model. However, since objects are defined using the clusters found by the first tier, we can only remove the object characterization part of this tier. In other words, in the OnlySecondTier method, we still continue using the objects defined by the first tier but categorize these objects with respect to only their discretized `dbs` values β_i.

4.2.3.5 AreaBasedSecondTier Method

In this method, the first tier identifies the pre-categories α_i of objects and then the second tier uses the objects' areas for their sub-categorization (i.e., this method also uses α_i defined by the first tier but employs the objects' areas instead of their `dbs` values). For area discretization, we quantize the area values of the objects located on the training images by the k-means algorithm and learn three

clustering vectors corresponding to small, medium and large objects. This is the same discretization procedure that we follow for the calculation of the `dbs` metric. Calculated quantization intervals for the area threshold[2] $T_{area} = 40$ are given in Table 4.1 and area histogram of training set objects is shown in Fig. 4.1.

Table 4.1: Quantization intervals for the area threshold $T_{area} = 40$. These intervals are automatically calculated on the training images.

T_{area}	Small	Medium	Large
40	area $\leq$ 4364	4365 $\leq$ area $\leq$ 23626	23627 $\leq$ area

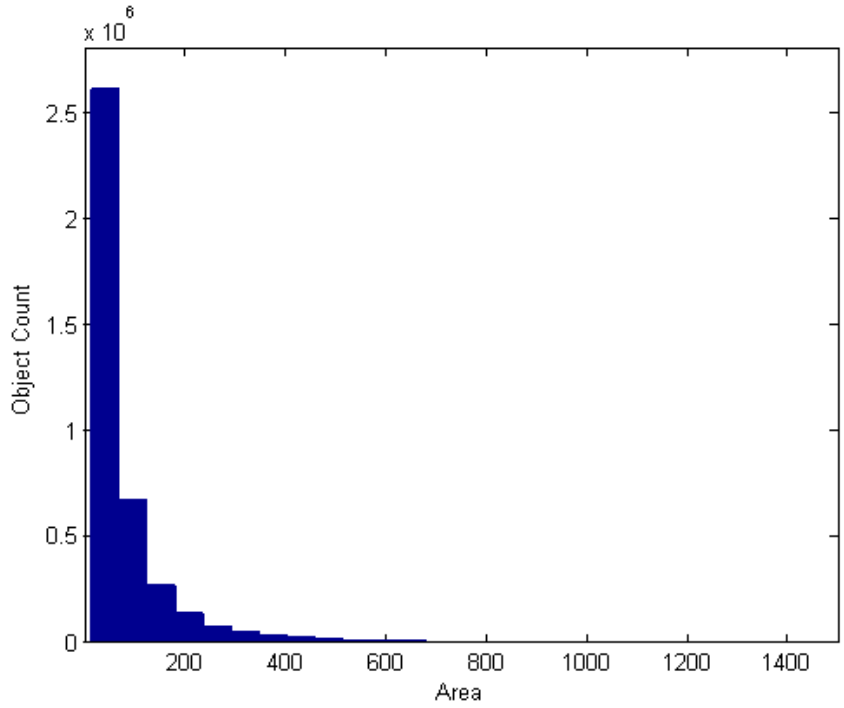

Figure 4.1: The histogram of training set objects' areas.

[2]Note that this area threshold is selected using cross-validation in the parameter selection process of two-tier model; thus we use the same threshold value for area the based model.

4.3 Parameter Selection

The proposed two-tier method has four external model parameters: cluster number K , area threshold T_{area}, covered pixel percentage c_{pixel}, and edge threshold T_{edge}. Besides, the support vector machine classifier has an additional parameter C. In our experiments, we select these parameters applying three-fold cross-validation on the training images. In particular, we consider different values of these parameters and select the combination for which three-fold cross-validation yields the highest class-based average accuracy. The sets of the parameter values that we consider are $K = \{2, 4, 6, 8\}$, $T_{area} = \{20, 30, 40, 50\}$, $c_{pixel} = \{1, 5, 10, 25\}$, $T_{edge} = \{10, 15, 20, 25\}$, and $C = \{0.005, 0.01, 0.05, 0.1, 0.5, 1, 2, \ldots, 10, 20, \ldots, 100\}$. The parameter values selected by cross-validation are $K = 6$, $T_{area} = 40$, $c_{pixel} = 5$, $T_{edge} = 20$, and $C = 0.01$. We also use a similar three-fold cross-validation method to select the parameter values for the comparison algorithms.

4.4 Test Results

We report the test set accuracies obtained by our proposed two-tier tissue decomposition model and the comparison methods in Table 4.2. Additionally, we give the confusion matrix of the two-tier model in Table 4.3. These tables show that the proposed model leads to high accuracies (> 93 percent) for all of the classes, also yielding the highest overall accuracy compared to the other methods. The pixel-based comparison methods represent an image by accumulating features defined at the pixel-level. Thus, they are more susceptible to noise, which is typically observed at the pixel-level in histopathological images. As seen in Table 4.2, this might be the main reason for these algorithms to give lower accuracies compared to the object-based methods, which do not directly use pixels in defining their features.

Among the object-based comparison methods, the *DelaunayTriangulation* algorithm, which represents an image with the distribution of only the nucleus

components, yields the lowest accuracies. This is attributed to the importance of defining multi-typed objects for image representation. As discussed earlier, the other object-based comparison methods also use multi-typed objects, which partially or entirely correspond to histological tissue components. However, to define these objects, they quantize image pixels into three clusters (corresponding to white, pink, and purple) based on the color information and then locate circles on each of these clusters. Different than these methods, our proposed model defines its objects, which may correspond to individual histological components but also subregions of different characteristics, by using the texture information in its first tier and the scale (size and shape) information in its second tier. The comparison results indicate the effectiveness of this new object definition.

We also report the test set accuracies obtained by modified versions of the proposed two-tier tissue decomposition model in Table 4.4. As seen in this table, based on the results of *SchmidFilterBankResponses* and *QuantizedPixels* methods, defining objects in the first-tier greatly improves the classification results. The second tier, which further categorizes the objects by using the proposed `dbs` metric, is also useful in obtaining higher accuracies especially for images of low-grade cancerous tissues. However, it is not sufficient to provide accurate classification results without texture information of the first tier. Finally the `dbs` metric is more effective than the area metric since it quantifies both the objects' shapes and sizes.

Table 4.2: Test set results of the proposed two-tier tissue decomposition model and the comparison methods.

	Normal	Low	High	Overall
Two-tier model	99.18	93.83	93.77	95.47
Object-based methods				
DelaunayTriangulation	89.61	71.56	87.55	79.71
ColorGraph [13]	92.67	82.46	86.38	86.24
GraphWalk [47]	93.48	90.40	92.61	91.71
HybridModel [14]	96.95	88.27	96.11	92.21
LocalObjectPattern [15]	95.32	92.54	90.27	93.03
Pixel-based methods				
IntensityHistogram	80.65	69.55	70.04	73.05
IntensityHistogramGrid	78.82	74.17	78.60	76.32
LocalBinaryPattern	92.67	73.46	80.54	80.53
CooccurrenceMatrix	83.10	81.64	77.82	81.47
GaborFilter	88.59	80.09	77.43	82.29
GaborFilterGrid	91.24	82.23	78.60	84.42
CooccurrenceMatrixGrid	87.58	84.12	85.60	85.43
RMM [45]	95.64	87.77	88.56	90.32

Table 4.3: The confusion matrix of the proposed two-tier tissue decomposition model for the test set.

		Computed		
		Normal	Low	High
Actual	Normal	487	4	0
	Low	2	792	50
	High	3	13	241

Table 4.4: Test set results obtained by the modified versions of the proposed two-tier tissue decomposition model.

	Normal	Low	High	Overall
Two-tier model	99.18	93.83	93.77	95.47
Modifications				
SchmidFilterBank	87.57	76.06	86.77	81.34
QuantizedPixels	91.85	86.02	87.94	88.13
OnlyFirstTier	97.96	89.57	92.60	92.65
OnlySecondTier	77.59	66.94	90.66	74.05
AreaBasedSecondTier	98.17	89.57	93.00	92.78

4.5 Parameter Analysis

We also analyze the effects of parameter selection on the performance of the proposed model. To this end, for each parameter, we fix the other parameters and measure the test set accuracies when different values of this parameter are used. We present the test set accuracies as a function of each parameter in Fig. 4.2 and Fig. 4.3.

4.5.1 Cluster Number K

It is the cluster number to which image pixels are quantized in the first tier. In our model, we find connected components on the pixels of each cluster to define objects and use objects' clusters to find their pre-categories. Thus, this parameter determines the objects used in representation as well as their types. Selecting smaller K values may result in defining single objects on the regions of different characteristics, decreasing classification accuracies. On the other hand, selecting larger values increases the number of the object types, which in turn increases the number of the edge types whose histogram will be used in feature extraction. As seen in Fig. 4.2(a), this slightly lowers the accuracies most probably due to curse-of-dimensionality.

4.5.2 Area Threshold T_{area}

The other parameter used by the first tier is the area threshold T_{area} to eliminate smaller connected components. Smaller threshold values cause to include spurious noisy objects into the representation whereas its larger values cause to eliminate some necessary objects. Both of these conditions decrease the accuracy, as observed in Fig. 4.2(b).

4.5.3 Pixel Percentage c_{pixel}

It is used in `dbs` calculation in the second tier. When it is selected too small, objects are covered by a filter in the very first iterations, regardless of their shapes and scales, and hence the calculated `dbs` values cannot differentiate the objects. In that case, the model converges to the OnlyFirstTier method, which we implemented for comparison purpose by removing the second tier from the model. Consistent with the comparison results provided in Table 4.4, such selection lowers the classification accuracy. Selecting a larger value for this percentage slightly affects the results, as given in Fig. 4.3(a). However, as this parameter affects the point where the iterations stop, larger values will make the `dbs` calculation unnecessarily long.

4.5.4 Edge Threshold T_{edge}

The edge threshold T_{edge} is the last parameter that the image representation/classification step is used to eliminate edge types with lower frequencies. Selecting too small values leads to using too much features in representation. This slightly reduces the accuracy, which is attributed to curse-of-dimensionality in classification. When it is selected too large, only few features are left in the representation and these features are not sufficient to accurately classify the images. Performance and feature vector size analysis of T_{edge} parameter is given in Fig. 4.3(b) and Fig. 4.4, respectively.

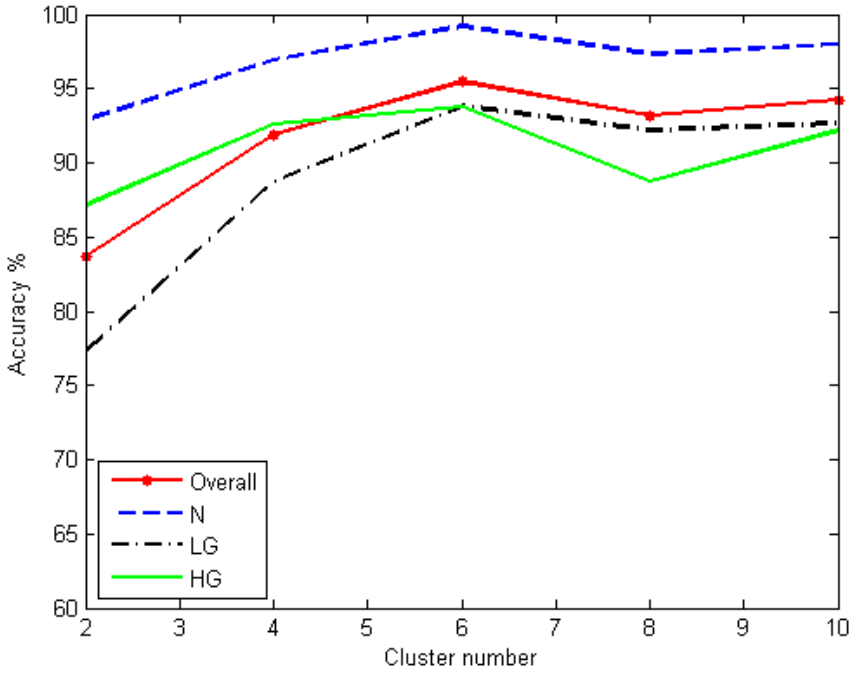

(a)

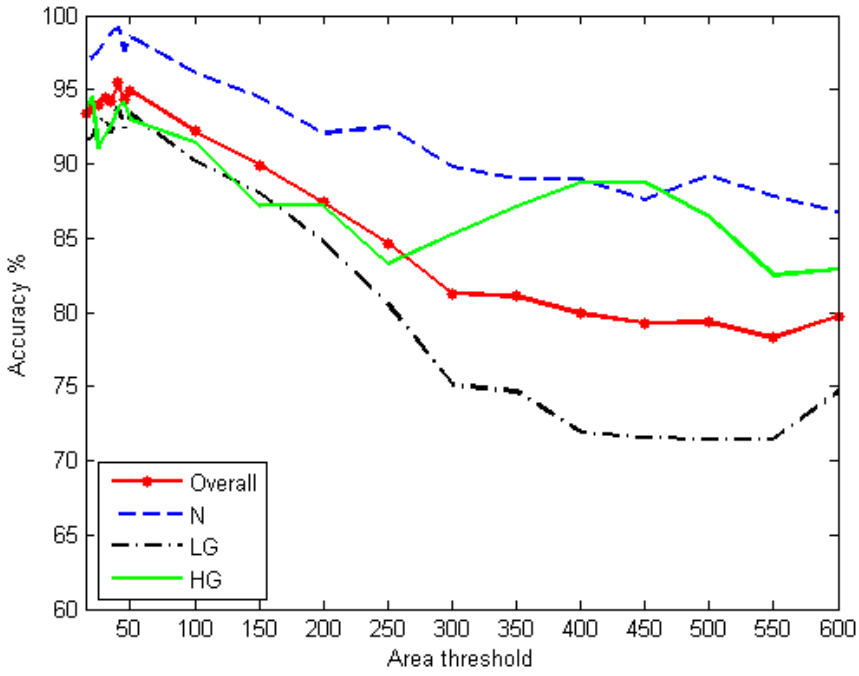

(b)

Figure 4.2: Parameter analysis; (a) cluster number K and (b) area threshold T_{area}.

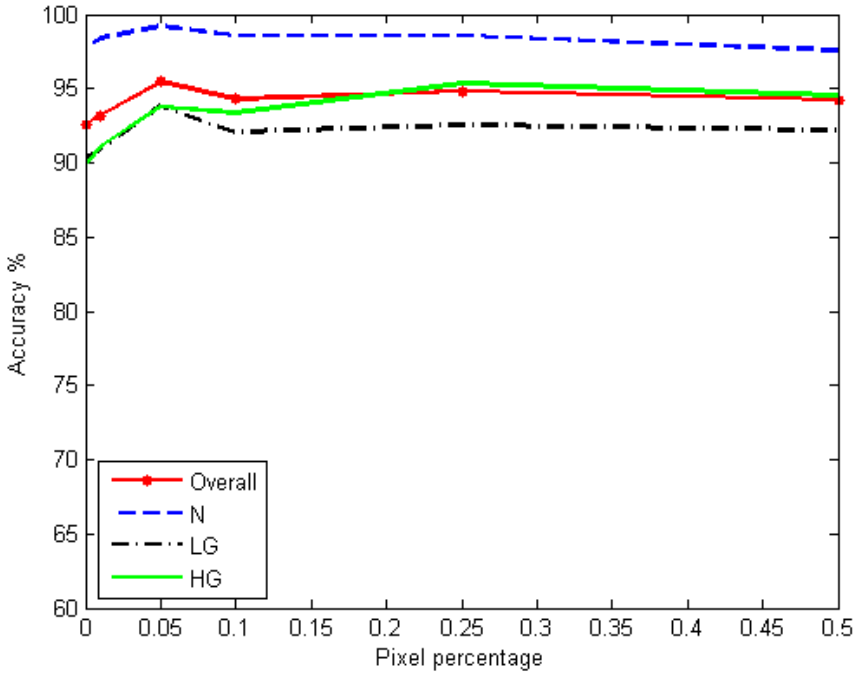

(a)

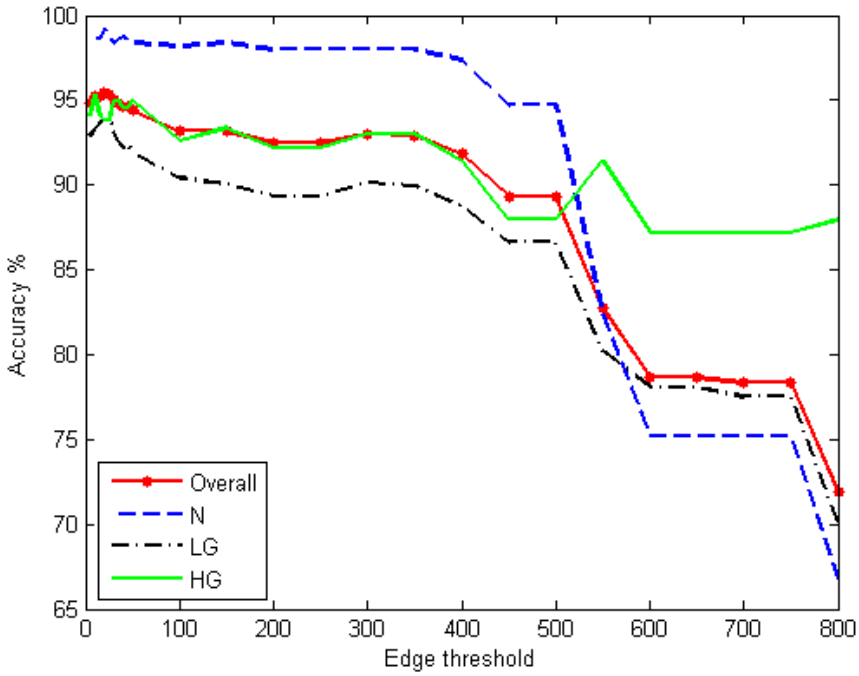

(b)

Figure 4.3: Parameter analysis; (a)pixel percentage c_{pixel} and (b) edge threshold T_{edge}.

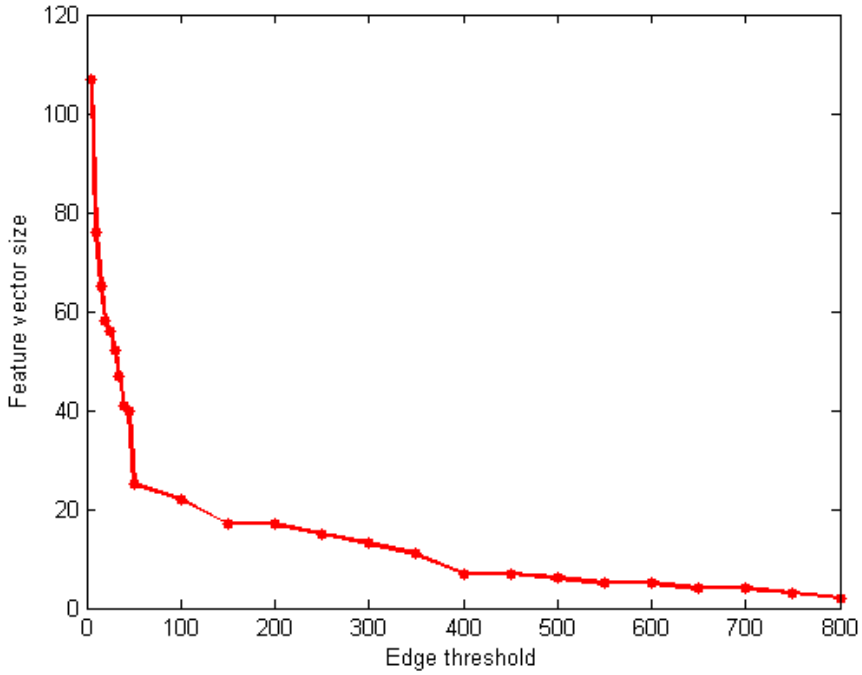

Figure 4.4: Feature vector size with respect to the edge threshold T_{edge}.

Chapter 5

Conclusion

In this study, we introduced a new two-tier tissue decomposition method for histopathological image characterization and classification. This method relies on first decomposing an image into a set of texturally similar local regions and then further categorizing these local regions based on their shape and size properties. For classification, it constructs a graph on the categorized regions and extracts the distribution of labeled graph edges. In that sense, this two-tier model combines textural, morphological and structural information and employs this combined information for classification.

We test our two-tier model on 3236 microscopic colon tissue images. Our experiments revealed that the categorized objects, which are defined using the proposed two-tier tissue decomposition model, provide more distinctive representations for cancer grading compared to the existing algorithms. Our experiments showed that the newly introduced dominant blob scale (`dbs`) metric for further categorization of local regions is useful.

The proposed image decomposition model has the potential to give successful results for different applications. For example, one can consider using the edge type histograms generated by this model to calculate image similarities for the purpose of retrievals. Alternatively, it is possible to directly use the generated graphs for similarity calculation. Exploring these similarity calculations could

be considered as one of the future research directions of this thesis. As another research direction, one could consider using the extracted features to merge over-segmented regions in tissue image segmentation. To this end, these features are extracted on the objects located in each segmented region and then these regions are merged based on the similarity between their extracted features.

In our previous work, we defined various texture measures on the circles located on the quantized pixels (i.e., on purple, pink, and white pixels). These textures can also be defined on the new objects characterized by the proposed tissue decomposition model. Since these new objects are defined considering the pixel texture, shape, and size information, it is expected to obtain better texture models. The investigation of such texture definitions could be considered as another future direction of this thesis.

Bibliography

[1] A. Jemal, R. Siegel, J. Xu, and E. Ward, "Cancer statistics, 2010," *CA: a Cancer Journal for Clinicians*, vol. 60, no. 5, pp. 277–300, 2010.

[2] A. Tabesh, M. Teverovskiy, H. Y. Pang, V. P. Kumar, D. Verbel, A. Kotsianti, and O. Saidi, "Multifeature prostate cancer diagnosis and gleason grading of histological images," *IEEE Transactions on Medical Imaging*, vol. 26, no. 10, pp. 1366–1378, 2007.

[3] F. Bunyak, A. Hafiane, and K. Palaniappan, "Histopathology tissue segmentation by combining fuzzy clustering with multiphase vector level sets," *Advances in Experimental Medicine and Biology*, vol. 696, pp. 413–424, 2011.

[4] A. N. Esgiar, R. N. G. Naguib, B. S. Sharif., M. Bennett, and A. Murray, "Microscopic image analysis for quantitative measurement and feature identification of normal and cancerous colonic mucosa," *IEEE Information Technology in Biomedicine*, vol. 2, no. 3, pp. 197–203, 1998.

[5] S. Doyle, M. Feldman, J. Tomaszewski, and A. Madabhushi, "A boosted bayesian multi-resolution classifier for prostate cancer detection from digitized needle biopsies," *IEEE Transactions on Medical Imaging*, vol. 59, no. 5, pp. 1205–1218, 2012.

[6] K. Jafari-Khouzani and H. Soltanian-Zadeh, "Multiwavelet grading of pathological images of prostate," *IEEE Transactions on Medical Imaging*, vol. 50, no. 6, pp. 697–704, 2003.

[7] S. Doyle, S. Agner, A. Madabhushi, M. Feldman, and J. Tomaszewski, "Automated grading of breast cancer histopathology using spectral clustering with textural and architectural image features," in *Proceedings of the 5th IEEE International Symposium on Biomedical Imaging: From Nano to Macro*, pp. 496 – 499, 2008.

[8] O. Sertel, J. Kong, H. Shimada, U. V. Catalyurek, J. H. Saltz, and M. Gurcan, "Computer-aided prognosis of neuroblastoma on whole slide images: classification of stromal development," *European Journal of Cancer*, vol. 42, no. 6, pp. 1093–1103, 2009.

[9] Y. Zhang, B. Zhang, F. Coenen, and W. Lu, "Breast cancer diagnosis from biopsy images with highly reliable random subspace classifier ensembles," *Machine Vision and Applications*, vol. 24, no. 7, pp. 1405–1420, 2013.

[10] A. N. Basavanhally, S. Ganesan, S. Agner, J. P. Monaco, M. D. Feldman, J. E. Tomaszewski, G. Bhanot, and A. Madabhushi, "Computerized image-based detection and grading of lymphocytic infiltration in her2+ breast cancer histopathology," *European Journal of Cancer*, vol. 57, no. 3, pp. 642–65, 2010.

[11] C. Demir, S. H. Gultekin, and B. Yener, "Learning the topological properties of brain tumors," *IEEE ACM Transactions on Computational Biology*, vol. 2, no. 3, pp. 262–270, 2005.

[12] B. Weyn, G. van de Wouwer, S. Kumar-Singh, A. V. Daele, P. Scheunders, E. van Marck, and W. Jacob, "Computer-assisted differential diagnosis of malignant mesothelioma based on syntactic structure analysis," *European Journal of Cancer*, vol. 35, pp. 23–29, 1999.

[13] D. Altunbay, C. Cigir, C. Sokmensuer, and C. Gunduz-Demir, "Color graphs for automated cancer diagnosis and grading," *IEEE Transactions on Biomedical Engineering*, vol. 57, no. 3, pp. 665–674, 2010.

[14] E. Ozdemir and C. Gunduz-Demir, "A hybrid classification model for digital pathology using structural and statistical pattern recognition," *European Journal of Cancer*, vol. 32, no. 2, pp. 474–483, 2013.

[15] G. Olgun, C. Sokmensuer, and C. Gunduz-Demir, "Local object patterns for tissue image representation and cancer classification," *IEEE Journal of Biomedical Health Informatics*, vol. (in press), 2014.

[16] T. Lindeberg, "Feature detection with automatic scale selection," *International Journal of Computuer Vision*, vol. 30, no. 2, pp. 79–116, 1998.

[17] D. G. Lowe, "Distinctive image features from scale invariant keypoints," *International Journal of Computuer Vision*, vol. 60, no. 2, pp. 91–110, 2004.

[18] K. S. Pedersen, M. Loog, and P. van Dorst, "Salient point and scale detection by minimum likelihood," in *Proceedings of the Journal of Machine Learning Research*, JMLR '07, pp. 59–72, 2007.

[19] M. Isard and J. MacCormick, "Bramble: a bayesian multiple-blob tracker," in *Proceedings of the IEEE International Conference on Computer Vision*, vol. 2 of *ICCV '01*, pp. 34–41, 2001.

[20] R. T. Collins, "Mean-shift blob tracking through scale space," in *Proceedings of the IEEE International Conference on Computer Vision and Pattern Recognition*, vol. 2 of *CVPR '03*, pp. 234–240, 2003.

[21] P. Forssen and A. Moe, "View matching with blob features," in *Proceedings of the Canadian Conference on Computer and Robot Vision*, CRV '05, pp. 228–235, 2005.

[22] J. Yang, J. Cheng, and H. Lu, "Human activity recognition based on the blob features," in *Proceedings of the IEEE International Conference on Multimedia and Expo*, ICME '09, pp. 358–361, 2009.

[23] Q. Xu and Y. Q. Cheng, "Multiscale blob features for gray scale, rotation and spatial scale invariant texture classification," in *Proceedings of the International Conference on Pattern Recognition*, ICPR '06, pp. 29–32, 2006.

[24] H. S. Sheshadri and A. Kandaswamy, "Experimental investigation on breast tissue classification based on statistical feature extraction of mammograms," *Computerized Medical Imaging and Graphics*, vol. 31, no. 1, pp. 46–48, 2007.

[25] P. Santago and H. Gage, "Quantification of mr brain images by mixture density and partial volume modeling," *IEEE Transactions on Medical Imaging*, vol. 12, no. 3, pp. 566–574, 1993.

[26] L. O. Martins, A. M. dos Santos, A. C. Silva, and A. C. Paiva, "Classification of normal, benign and malignant tissues using co-occurrence matrix and bayesian neural network in mammographic images," in *Proceedings of the Ninth Brazilian Symposium on Neural Networks*, SBRN '06, 2006.

[27] M. McNitt-Gray, N. Wyckoff, J. Sayre, J. Goldin, and D. Aberle, "The effects of co-occurrence matrix based texture parameters on the classification of solitary pulmonary nodules imaged on computed tomography," *Computerized Medical Imaging and Graphics*, vol. 23, no. 6, pp. 339–348, 2006.

[28] R. Haralick, K. Shanmugam, and I. Dinstein, "Quantification of mr brain images by mixture density and partial volume modeling," *IEEE Transactions on Systems, Man and Cybernetics*, vol. 3, no. 6, pp. 610–621, 1973.

[29] T. Leung and J. Malik, "Representing and recognizing the visual appearance of materials using three-dimensional textons," *International Journal of Computer Vision*, vol. 43, no. 1, pp. 29–44, 2001.

[30] A. Mojsilovic, M. Popovic, A. Neskovic, and A. Popovic, "Wavelet image extension for analysis and classication of infarcted myocardial tissue," *IEEE Transactions on Biomedical Engineering*, vol. 44, no. 9, pp. 856–866, 1997.

[31] M. Hussain, S. Khan, G. Muhammad, and G. Bebis, "A comparison of different gabor features for mass classification in mammography," in *Eighth International Conference on Signal Image Technology and Internet Based Systems*, SITIS '12, pp. 142–148, 2012.

[32] Z. Lei, T. Fang, H. Huo, and D. Li, "Bi-temporal texton forest for land cover transition detection on remotely sensed imagery," *IEEE Transactions on Geoscience and remote sensing*, vol. 52, no. 2, pp. 1227–1237, 2014.

[33] M. Gangeh, A. Sadeghi-Naini, M. Kamel, and G. Czarnota, "Assesment of cancer therapy effects using texton-based characterization of quantitative

ultrasound parametric images," in *IEEE 10th International symposium on biomedical imaging*, ISBI '13, pp. 1372–1375, 2013.

[34] T. Ojala, M. Pietikinen, and D. Harwood, "Performance evaluation of texture measures with classification based on kullback discrimination of distributions," in *Proceedings of the 12th IAPR International Conference on Pattern Recognition*, vol. 1 of *ICPR '94*, pp. 582–585, 1994.

[35] Y. Fang and Z. Wang, "Improving lbp features for gender classification," in *International Conference on Wavelet Analysis and Pattern Recognition*, vol. 1 of *ICWAPR '08*, pp. 373–377, 2008.

[36] G. Liasis, C. Pattichis, and S. Petroudi, "Combination of different texture features for mammographic breast density classification," in *IEEE 12th International Conference on Bioinformatics and Bioengineering*, BIBE '12, pp. 732–737, 2012.

[37] B. B. Mandelbrot, "The fractal geometry of nature," *ISBN: 978-0-7167-1186-5*, 1983.

[38] J. Z. Liu, L. D. Zhang, and G. H. Yue, "Fractal dimension in human cerebellum measured by magnetic resonance imaging," *Biophysical Journal*, vol. 85, no. 6, pp. 4041–4046, 2003.

[39] R. D. King, A. T. George, T. Jeon, L. S. Hynan, T. S. Youn, D. N. Kennedy, and B. Dickerson, "Characterization of atrophic changes in the cerebral cortex using fractal dimensional analysis," *Brain Imaging and Behaviour*, vol. 3, no. 2, pp. 154–166, 2009.

[40] H. Choi, T. Jarkrans, E. Bengtsson, J. Vasko, K. Wester, P. Malmstrom, and C. Busch, "Image analysis based grading of bladder carcinoma. comparison of object, texture, and graph based methods and their reproducibility.," *Analytical Cellular Pathology*, vol. 15, no. 1, pp. 1–18, 1997.

[41] S. Doyle, M. Hwang, K. Shah, A. Madabhushi, M. Feldman, and J. Tomaszeweski, "Automated grading of prostate cancer using architectural and textural image features.," in *IEEE 4th International Symposium*

on Biomedical Imaging: From Nano to Macro, BIBE '12, pp. 1284–1287, 2007.

[42] K. Mikolajczykm and C. Schmid, "Scale and affine invariant interest point detectors," *International Journal of Computer Vision*, vol. 60, no. 1, pp. 63–86, 2004.

[43] C. Schmid, "Constructing models for content-based image retrieval," in *Proceedings of the IEEE International Conference on Computer Vision and Pattern Recognition*, vol. 2 of *CVPR '01*, pp. 39–45, 2001.

[44] P. Kovesi, "Code for convolving an image with a bank of log-gabor filters," in *Available at http://www.csse.uwa.edu.au/p̃k/ Research/MatlabFns/ PhaseCongruency/gaborconvolve.m.*

[45] E. Ozdemir, C. Sokmensuer, and C. Gunduz-Demir, "A resampling based markovian model for automated colon cancer diagnosis," *IEEE Transactions on Biomedical Engineering*, vol. 59, no. 1, pp. 281–289, 2012.

[46] Y. Deng and B. S. Manjunath, "Unsupervised segmentation of color-texture regions in images and video," *IEEE Transactions on Pattern Analysis and Machine Intelligence*, vol. 23, no. 8, pp. 800–810, 2010.

[47] G. Olgun, C. Sokmensuer, and C. Gunduz-Demir, "Graph walks for classification of histopathological images," in *Proceedings of the Biomedical Imaging: From Nano to Macro*, ISBI '13, 2013.